5-2016

Synthetic Aperture Radar Interferometry Analysis of Ground Deformation within the Coso Geothermal Site, California

Erik Vaughn Brawner
University of Arkansas, Fayetteville

Synthetic Aperture Radar Interferometry Analysis of Ground Deformation within the Coso Geothermal Site, California

A thesis submitted in partial fulfillment
of the requirements for the degree of
Master of Science in Geology

by

Erik Brawner
Western Illinois University
Bachelor of Science in Geology, 2012

May 2016
University of Arkansas

This thesis is approved for recommendation to the Graduate Council.

_____
Dr. Mohamed Aly
Thesis Director

_____
Dr. Jackson Cothren
Committee Member

_____
Dr. Gregory Dumond
Committee Member

Abstract

Earth's surface movement may cause as a potential hazard to infrastructure and people. Associated earthquake hazards pose a potential side effect of geothermal activity. Modern remote sensing techniques known as Interferometric Synthetic Aperture Radar (InSAR) can measure surface change with a high degree of precision to mm scale movements. Previous work has identified a deformation anomaly within the Coso Geothermal site in eastern California. Surface changes have not been analyzed since the 1990s, allowing a decade of geothermal production impact to occur since previously assessed. In this study, InSAR data was acquired and analyzed between the years 2005 and 2010. Acquired by the ENVISAT satellite from both ascending and descending modes. This provides an independent dataset from previous work. Incorporating data generated from a new sensor covering a more modern temporal study period. Analysis of this time period revealed a subsidence anomaly in correlation with the extents of the geothermal production area under current operation. Maximum subsidence rates in the region reached approximately 3.8 cm/yr. A similar rate assessed from previous work throughout the 1990s. The correlation of subsidence patterns suggests a linear source of deformation from measurements spanning multiple decades. Regions of subsidence branch out from the main anomaly to the North-Northeast and to the South where additional significant peaks of subsidence occurring. The extents of the deformation anomaly directly correlate with the dispersal of geothermal production well site locations. Depressurization within the geothermal system provides a leading cause to surface subsidence from excessive extraction of hydrothermal fluids. As a result of minimal reinjection of production fluids.

Acknowledgements

The completion of this thesis is due to the continued guidance and support of faculty, friends and family members throughout this process.

Many thanks are owed to Dr. Mohamed Aly who served as my advisor and thesis committee chair. He has provided continual guidance towards the formation of this work and throughout the numerous steps required for completion of this thesis. He has provided continual support my academic endeavors here at the University of Arkansas that has allowed me to continue focus on this research at hand.

I would like to thank the Arkansas Space Grant Consortium (ASGC) and NASA EpSCOR for financial assistance that has allowed me to continue my focus on this work. The European Space Agency for providing the Synthetic Aperture Data (SAR) generated from the ENVISAT satellite mission. The Jet Population Laboratory for elevation data (SRTM) and the United States Geological Survey (USGS) for providing seismic data.

I would like to thank my parents Mike and Jackie Brawner who have continued to push me to academic goals that would have otherwise not been achieved. As well as the never ending support to remind myself that I am capable of undertaking such tasks.

Contents

List of Tables

List of Figures

Chapter 1

Introduction

The Coso geothermal area is a constantly developing system in a significant tectonically active region. Natural and human-induced processes within the geothermal system can inhibit frequent and potentially dangerous seismicity. Utilization of advanced remote sensing techniques known as Interferometric Synthetic Aperture Radar (InSAR), provide an ability to accurately model and understand the factors at play within an active geothermal system in the region and the interplay with seismic events. In an attempt to study the active geothermal processes and seismic events occurring at the Coso geothermal site, this thesis will address the impacts that these occurrences have with the local crustal deformation. Geodetic data from Interferometric Synthetic Aperture Radar (InSAR) can be utilized to model deformation trends throughout the region.

1.1 Study Site

The Coso geothermal area occurs within the Naval Air Weapons Station at China Lake in eastern California. This area is a part of the Coso Range located at the southern extent of the Owens Valley between the Sierra Nevada Mountains to the West and the Argus Range to the East (Figure 1.1). The total study area is contained within a bounding box of North latitude 36.181488°, South latitude 35.879579°, W longitude -117.933384°, and East longitude -117.682265. The region exhibits an arid climate on the backside of the Sierra Nevada crest. Land cover within this arid climate consists predominantly of desert scrub as a result of precipitation amounts accumulating to a few inches per year.

The region is heavily impacted by tectonic influences associated with the plate movement interactions between the Pacific plate in relation to the North American plate occurring on both sides of the Coso region. Extensive faulting within the region as a result of these influences has created an environment for the existence of a geothermal system within these faults and fractures. Geothermal production practices began in 1987 and continue today. The combination of fluid injection practices and the natural instability of a tectonically active region contribute to one of the highest seismically active regions in Southern California (Walter and Weaver, 1980).

1.2 Geological Setting

The Coso Range and surrounding region has undergone multiple episodes of volcanic activity within the previous 4 Ma (Duffield et al, 1980) that has shaped the geological characteristics of the region. The Coso Range and more specifically the volcanic area containing the geothermal field are constructed primarily of a Mesozoic Basement complex overlain by a patchy veneer of volcanic rocks emplaced from volcanic episodes of Pliocene and Pleistocene age. The basement complex consists of granitic plutons, dioritic to gabbroic plutons and metamorphic rocks (Duffield et al, 1980). This complex has been moderately faulted and fractured as a result of extensional tectonics of the region. These faults in turn create the structure for the existence of the geothermal system within the fractures due to increased permeability.

During time of increased activity in the last 4 my, approximately 35 cubic km of volcanic rock has been erupted and emplaced (Duffield et al, 1980; Bacon et al, 1980). This volcanic rock can predominantly be associated within two epochs of eruption time throughout the Pliocene and Pleistocene. The oldest units associated with Pliocene age activity consist of basalt flows. Basalt

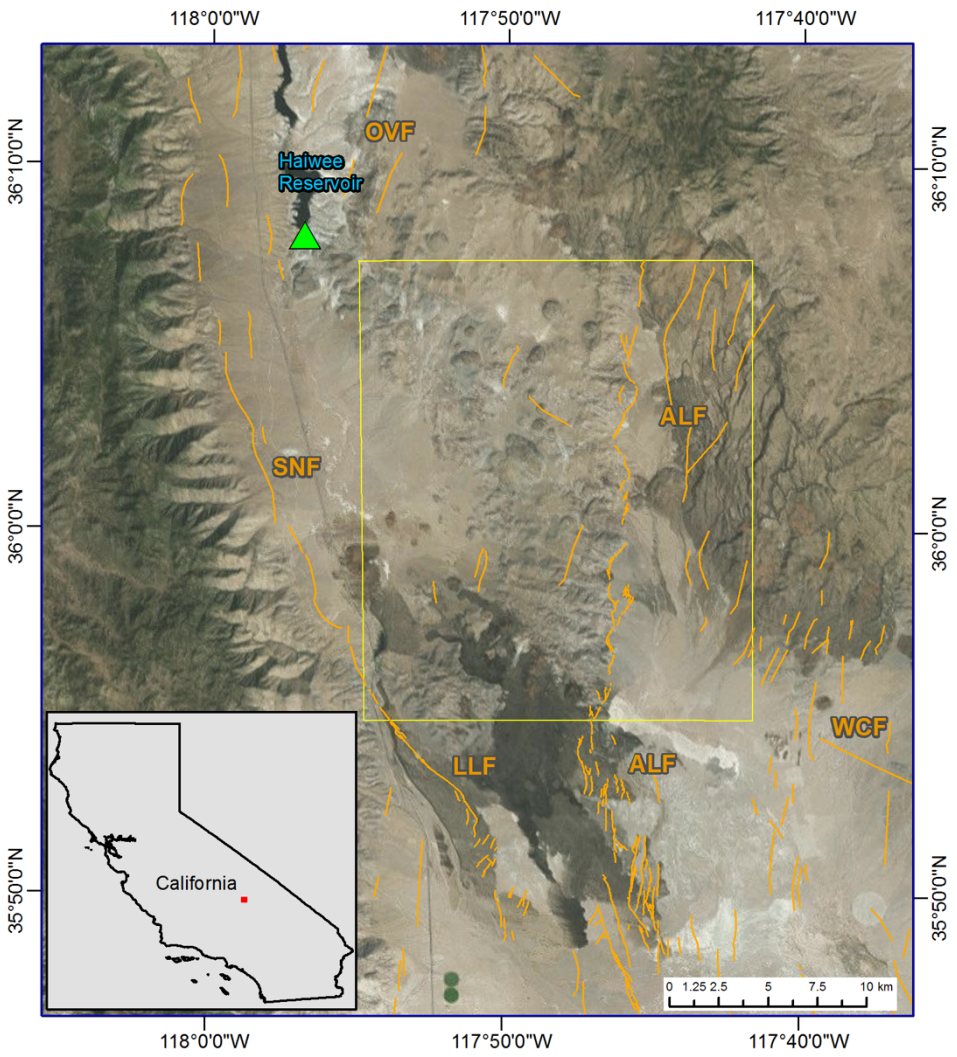

Figure 1.1: Location map of the Coso geothermal area. The yellow box represents the boundaries of the Coso geothermal study area. The green triangle marks the location of the Haiwee Reservoir Climate Station (UofCal, 2014). The orange lines represent the Quaternary faults within the region courtesy of (U.S. Geological Survey, 2006). OVF stands for the Owens Valley fault system. LLF stands for the Little Lake fault system. ALF stands for the Airport Lake fault system, SNF stands for the Sierra Nevada Frontal Fault and WCF stands for the Wilson Canyon Fault. Aerial imagery courtesy of (ESRI, 2016).

makes up the most abundant deposits within the Coso Range. One of these significant deposits results in the step faulted terrane east of the Coso hot springs that is underlain by these basaltic emplacements (Duffield et al, 1980). Other characteristic deposits of the Pliocene consist of andesite, dacite, rhyodacite as air-fall pumice and lava flows and rhyolite as a pumiceous ash flow tuff.

The Pleistocene age deposits are characterized as basalt and rhyolite eruptions. These deposits are assumed to be emplaced within the last 1.1 my. Rhyolite deposits are generally younger than their basaltic counterparts (Duffield et al, 1980). The most notable form of deposits for this time are the 38 rhyolite domes that characterize the landscape of the Coso volcanic field. Sugarloaf Mountain is the largest of these domes located at the center of the volcanic field. It is composed of a composite body of flows and domes roughly in the center of the volcanic field. All rhyolitic domes have been dated predominantly younger than 0.15 my (Duffield et al, 1980).

Methods of emplacement for much of the volcanic flows and specifically Pleistocene rhyolite in the region are said to be of dike emplacement (Bacon et al, 1980). Bacon et al (1980) suggest that timing and heat content within the system would support the ascent of magma vertically from beneath the center of the rhyolite field where the largest volume of volcanic rocks has been emplaced. Within this volcanic zone, a magma reservoir exists at depth that has provided a source energy to all of the volcanic rock emplacements excluding the oldest rhyolite of Pliocene age. Bacon et al (1980) suggest that the magma rose through the paths of dikes and provided source to even the extrusions on the outer perimeter of the volcanic field via offshoot dikes seen presently by the multitude of rhyolite domes within the volcanic field.

Multiple studies have sought to determine the source at depth driving the geothermal system (Bacon et al, 1980; Duffield et al, 1980; Monastero et al, 2005; Pluhar et al, 2006;

Reasenberg et al, 1980). Reasenberg et al (1980) suggest evidence for a low-velocity body beneath the Coso geothermal area as an elongated body that is approximately 5 km in width. They suggest the presence of a partial melt buried beneath the Coso geothermal area, that is supported by seismic data (Walter and Weaver, 1980) where it is confined within the upper 8 to 10 km suggesting ductile nature below 10 km. Combs (1980) also suggested the existence of a crustal magma body likely to exist at a depth between 5-20 km from teleseismic P wave analysis. Common ideas associate this body to supply heat to the fractured nature of the Basement complex within the Coso Range. Fracture density within the Basement complex can in turn provide the primary fluid-flow paths within the geothermal system where liquid is super heated.

1.3 Tectonic Setting

The Coso Range resides within a region bounded by the Sierra Nevada to the West and the Argus Range to the East. This region is greatly impacted by the North American-Pacific plate movements. Here, approximately 50 km north of the Garlock Fault, is a regional feature known as the Eastern California Shear Zone (ECSZ), which plays a large role in the balance between plate motion and the impact that the San Andreas Fault activity has to the West (Miller et al, 2001). The ECSZ has been said to account for approximately 19-28 percent of the relative plate motion that is associated with the North American and Pacific plate interactions (Miller et al, 2001). The ECSZ constitutes a region of right lateral strain partitioned into six domains broken up by the major strike slip faults and extensional zones determined by Dokka and Travis (1990). Faults within the ECSZ have become active within approximately 6 to 10 Mya. The broad network of strike slip faulting occurring in this region results from a broad distribution of regional dextral shear accounting for approximately 65 km of right lateral since formation. Right

lateral movement with the similar strike slip faulting that occurs within the Death Valley region creates this regional zone of dextral shear (Dokka and Travis, 1990).

As a result of these tectonic influences and dextral shearing throughout the region, significant faulting has occurred and continues to influence the processes throughout the Coso geothermal area. The order of faulting can be associated by the interaction of tectonic influences placed on the Coso Range where the seismotectonics of the region reflect the strike slip faulting of the San Andreas to the West and extensional faulting influenced by the Basin and Range to the East (Bhattacharyya and Lees, 2002).

The Coso Range sits within a releasing stepover of the ECSZ between the Indian Wells valley and the Wild Horse Mesa (Monastero et al, 2005). Creating this stepover, the Airport Lake fault zone proceeds north from the Garlock Fault where it splits into two distinct fault zones (Figure 1.1). To the west, the Little Lake fault zone proceeds along the Sierra Nevada front ultimately linking to the Owens Valley fault zone north of the Coso Range. Motion of the Sierra Nevada is predominantly to the Northwest at approximately 13-14 mm/yr. The eastern split of the Airport Lake fault zone can be traced along the western margin of the Coso Wash that feeds part of the shearing partitioned into the Wild Horse Mesa (Lewis, 2007). East of the Wild Horse Mesa, the predominant motion is to the Southeast.

The Coso Range is bounded to the east by the Wild Horse Mesa where it is separated by the Coso Wash fault zone. Our study area, the Coso geothermal area resides on the footwall to the west of this zone, amongst the horst and graben structure of the region (Pluhar et al, 2006). Here, Monastero et al (2005) suggest that the geothermal activity in the area is a result of a nascent metamorphic core complex below a detachment system at 3-4 km depth. Monastero et al (2005) suggest that the Coso field necessitates crustal thinning to accommodate horizontal plane-

strain transtension. The crustal thinning is accomplished as a result of brittle faulting on high angle and low angle normal faults that reside within the upper 4 km of crust. They conclude that the metamorphic core complex at the Coso geothermal area is very immature in age and will likely continue to be an actively forming structure for at least the next 2-4 my.

Faulting throughout the Coso Range accommodates the northwest striking dextral shear as imposed by the processes of the ECSZ. Regional Global Position System (GPS) data have shown that between the years 1993 to 2000, the Coso Range and immediate areas surrounding it have shown an average rate of dextral shearing of 6.5 ± 0.7 mm/yr throughout the Coso Range and Indian Wells Valley. Within the Coso Range faulting has been found to take the form of three dominantly trending fault sets all active in late Cenozoic time. The first set of faults are west-northwest to northwest trending faults of strike slip character (Duffield et al, 1980) that display vertical dip. These faults are well developed within the southern and western areas of the Coso Range. The northwest trending faults offset the Mesozoic basement complex as well as some Cenozoic volcanic rocks (Duffield et al, 1980; Bacon et al, 1980). The second set of faults are north trending normal faults (Duffield et al, 1980) with dips of 60°-70° east or west. These faults are well developed throughout most of the Coso Range (Bacon et al, 1980). The third set of faults within the Coso Range, consist of arcuate faults. These faults are predominantly a local phenomenon to the northern and northeastern parts of the volcanic field (Bacon et al, 1980).

1.4 Recent Seismicity

Extensive faulting and continued movement within the Coso range contributes to the presence of significant earthquakes. During the period of 1992 to 2015 in and around the Coso geothermal field, over 40,000 earthquake occurrences were recorded as shown in Figure 1.2

(SCEDC (2015)). The majority of the earthquakes that occur in the region are classified as micro-seismicity and up to small (M < 3.0) occurrences (Figure 1.3). Amongst the micro-seismicity, periodically large earthquake occurrences in excess of magnitude 4.9 occur in approximately 20 year intervals (Bhattacharyya and Lees, 2002). A 12.5 year period preceding geothermal production operations (1975-1987) in the Coso area exhibited a total count for earthquake occurrences of 9601 (SCEDC (2013)). This supports a correlation that geothermal production practices within the region have contributed to a significant increase in seismicity over the last <30 years of production.

Seismicity experienced within the geothermal area can be attributed to natural processes of rupture along faults as a result of tectonic processes, as well as the influence from injection of production fluids (Kaven et al, 2011). Feng and Lees (1998) state that fluid injection can increase the pore pressure and reduce effective stress within the system that likely creates local stress perturbations within the Coso geothermal area and activates faulting along the major pre-existing fractures. Within the geothermal area, Feng and Lees (1998) found that the indication of high preexisting fracture densities was correlated with high areas of seismicity. This suggests the likelihood that the fluid paths driving the geothermal system are located along these faults.

1.5 Climate Setting and Precipitation

Extensive studies of the climate (Danskin, 1998) have been performed in the Owens Valley to the North of the Coso Range. The Owens Valley vastly shares a similar climate to the Coso geothermal area as the two regions share physiogeographic boundaries and similar characteristics as the valley floor within the Owens Valley. The Coso Range acts as a barrier to water flow at the South end of the Owens Valley where it impedes outflow of groundwater from

the lower extent (Danskin, 1998).

The climate of the Coso Range much like the Owens Valley is greatly impacted by the presence of the Sierra Nevada Mountains directly to the West. Shadowed by the Sierra Nevada Mountains, the Coso region is influenced significantly by continental mass forces as an interior climate unlike the oceanic influences that impact a much larger portion of California from the Pacific Ocean (California Climate Zone 14). The region is characterized by low annual precipitation, moderate to low humidity and high potential evapotranspiration in vegetated areas that are predominantly covered in desert scrub (Danskin, 1998). These settings create a semiarid to arid environment that is characteristic of a high desert basin.

Temperature patterns in a high desert basin like the Coso Range consist of hot dry summers and cold winters. These temperatures also experience wide swings in range between the summer and winter months as well as daily temperature occurrences (California Climate Zone 14). Monthly average temperatures are illustrated in Figure 1.4. These averages show the range of temperatures experienced between the cold winter months that are capable of falling to temperatures below 0°F (Danskin, 1998) and heating up to temperatures exceeding 110°F in the summer months.

Temperature and low relative humidity coupled with topographic constraints create a region that experiences rain or snow that amounts to less than an inch per month (California Climate Zone 14). The orographic effect of the Sierra Nevada creates a rain shadow effect over the Coso region decreasing the precipitation accumulation experienced greatly from that West of the Sierra Nevada crest (Danskin, 1998). Illustrated in Figure 1.5, precipitation values per month are very low generally not exceeding 1 inch. This precipitation accounts for approximately 3 to 12 inches per year.

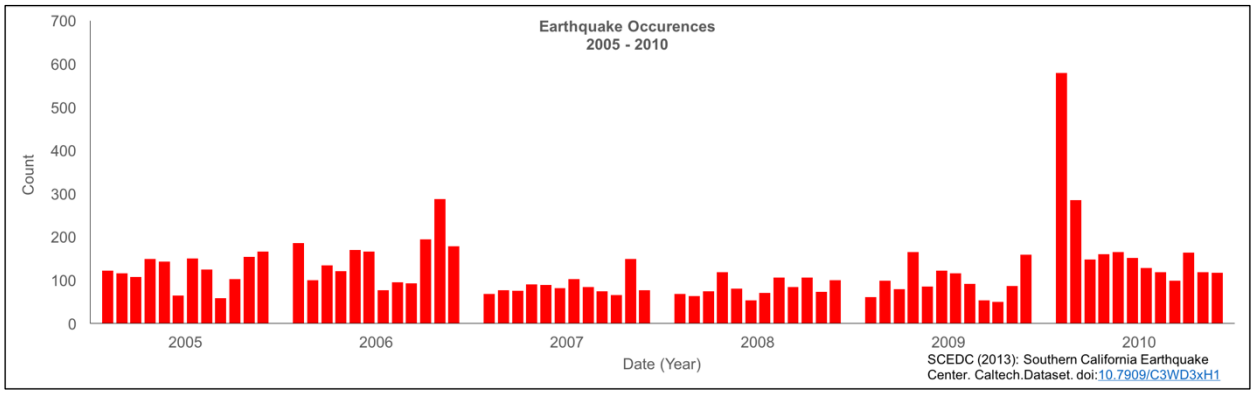

Figure 1.2: Earthquake occurrences in the Coso region between the years 1992 to April 2015. The Y axis represents the total number of earthquake occurrences. The X axis is divided as the months of successive years throughout study period. Data courtesy of (SCEDC, 2013).

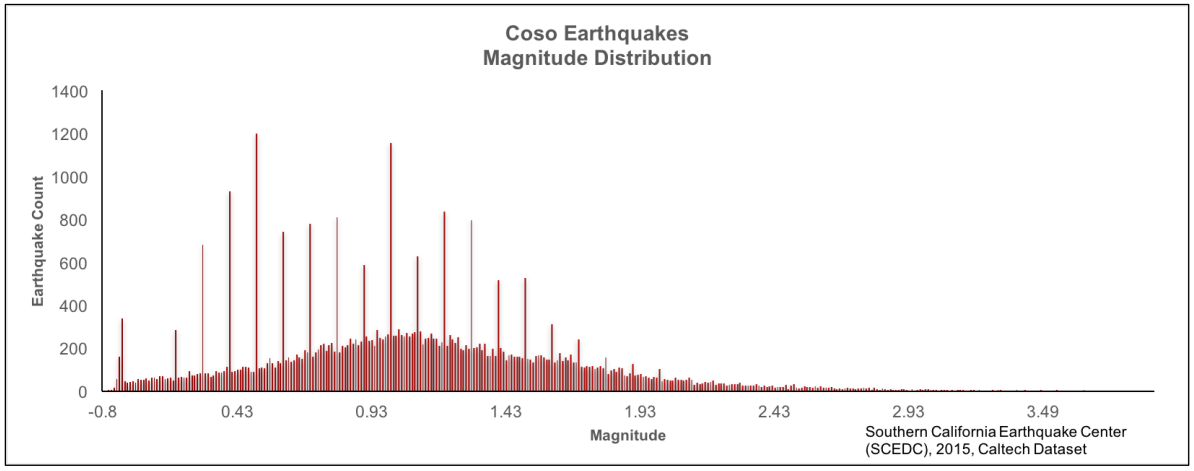

Figure 1.3: Earthquake magnitude distribution is displayed for earthquake occurrences within the Coso geothermal area. The Y axis represents the total number of earthquakes that fell within designated magnitude intensity. The X axis represents the range of magnitude intensities that occurred within the region. Data courtesy of (SCEDC, 2013).

An important factor in the amount of water within the hydrologic system in the Coso region is a process known as evapotranspiration. Evapotranspiration is the sum of evaporation and plant transpiration from the Earth's land and ocean surface to the atmosphere. Duell (1990) studied this process within the Owens Valley to the North of the Coso Range. Here he showed that evapotranspiration rates on the valley floor ranged from about 12 inches per year to about 45 inches per year. These rates were also dependent on the type and percentage of vegetative cover with the most evapotranspiration occurring within regions of native vegetation. These rates greatly exceed the amount of precipitation experienced in the Owens Valley floor and the Coso region by as much as 3 to 6 times (Duell, 1990). Within the vegetated areas, the ground water recharge of the region is heavily impacted by the quantity of water that is used by the overlying vegetation (Danskin, 1998).

1.6 Groundwater and System Recharge

The hydrologic region the Coso area resides within is known as the South Lahontan hydrologic region. This area spans from Owens Valley in the North to Indian Wells Valley in the South. The area within proximity to the Coso Range consists of three groundwater basins characterizing groundwater flow. The first of these groundwater basins is a 390,000 acre feet capacity basin known as the Coso Valley groundwater basin (Coso Valley Groundwater Basin, 2004). This basin is located southeast of the Coso volcanic field where it is recharged from the runoff of the surrounding highlands of the Argus and Coso Ranges. The runoff serves as a recharge for the basin by percolating through alluvial fan deposits at the base of the ranges (Coso Valley Groundwater Basin, 2004).

The second groundwater basin of the region is the Rose Valley Groundwater

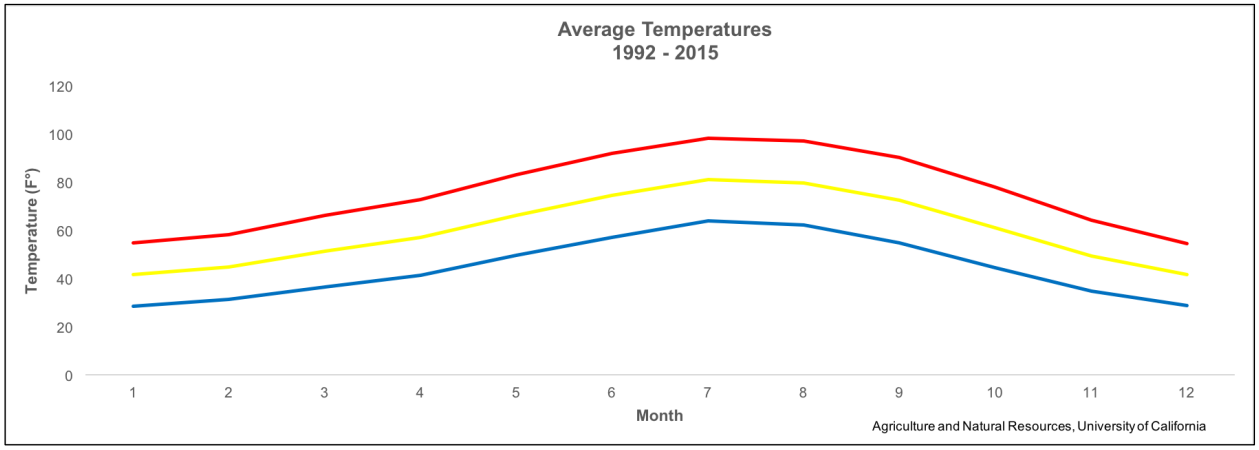

Figure 1.4: Monthly average temperature 1992 to April of 2015. The red line represents daily maximum values. The yellow line represents daily average temperatures. The blue line represents daily minimum temperatures. The temperatures were recorded at the Haiwee Reservoir. Data courtesy of (UofCal, 2014).

Basin. This basin has a total storage capacity of 820,000 acre feet (Rose Valley Groundwater Basin, 2004). The Rose Valley Basin is located West-southwest of the Coso volcanic field. At this location the basin is recharged from runoff of the Sierra Nevada Mountains to the West and the Coso Range to the East.

The third and largest of basins within the region is known as the Indian Wells Valley groundwater basin. This basin is located to the South of the Coso Range and the Coso Valley groundwater basin. The basin has a total storage capacity of approximately 5,120,000 acre feet (Indian Wells Valley Groundwater Basin, 2004). Like the previous basins the Indian Wells basins is recharged from runoff of high altitude surroundings. The Indian Wells basin is recharged primarily by runoff from the Sierra Nevada Mountains to the West and a smaller contributing factor of rainfall amounting to approximately 4-6 inches per year (Indian Wells Valley Groundwater Basin, 2004).

Each basin within the region displays a classic basin and range form of recharge for groundwater systems. Maxey (1968) defined this classic form of recharge as a process of runoff from high altitude or mountainous regions (recharge areas) to low altitude areas within the adjacent valleys (discharge areas). Guler and Thyne (2004) were able to demonstrate this recharge process for the Indian Wells Valley through hydrochemical analysis of the water at various stages through its discharge cycle. They showed the passage through five phases represented by clusters starting at Group-1 as precipitation and snow runoff from the Sierra Nevada Mountains. It then passes through the basin-fill aquifer, typically the lower slopes of the Sierra Nevada and Coso Range. This is shown as the major-ions significantly increase as the groundwater interacts with the basin-fill deposit minerals of the region. Significant to the Coso Range, the water is potentially affected by geothermal leakage before ultimately evolving into

discharge area waters in their designation of Group-4 and Group-5 phases of groundwater clusters.

A form of recharge to the Coso geothermal system is relatively unknown, while the source of geothermal fluids has been suggested to derive from meteoric waters of the Sierra Nevada and Coso Ranges (Fournier and Thompson, 1980; Williams and McKibben, 1990). A change to the dry and arid climate has altered the fluid flow within the geothermal system. Adams et al (2000) states, that the earlier phases of geothermal development (>10 ka) were recharged by a low-salinity, non-thermal groundwater system.

1.7 Hydrothermal Activity

The approximately 30 square km geothermal system present within the Coso area has recorded activity for at least the last 300 ka. This geothermal field is located between Rose Valley to the West and the Coso Wash to the East. Activity continues in modern time displaying associated surface manifestations that primarily take place on or near the Coso Wash Fault (Coso Operating Company, 2008). The extensive faulting and fracturing within the region is the controlling factor of fluid flow within the geothermal system as this principally liquid-dominated system is heated by a shallow magma source associated with the brittle ductile transition zone at approximately 5 km. Davatzes and Hickman (2005) analyzed fault hosted fluid flow within the Coso geothermal field. They attributed the distribution of active fumaroles, surface alteration and steam ejection as an indicating factor of fluid flow along active fault segments trending NNE and at intersections between fault segments by the indication of perturbations in borehole temperature logs.

Adams et al (2000) define that the geothermal system has experienced three distinct

episodes of thermal activity. The first episode of activity began approximately 307 ka with an above moderate temperature system producing travertine deposits on the eastern side of the field. The second episode of activity marks sinter deposits at approximately 238 ka driven by magmatic activity within the volcanic field. This period marks an increase in temperature exceeding 200°C (Adams et al, 2000). Travertine deposits have been observed as networks of veins that have filled fractures within the basement complex (Duffield et al, 1980). The travertine and some sinter deposits were emplaced prior to basaltic eruptions within the Pleistocene. The timing of activity suggests the association of a magmatic body directly heating the system prior to eruption (Duffield et al, 1980). The modern hydrothermal field is partitioned into three weakly connected or isolated reservoirs. These reservoirs are distinguishable by their differences in temperatures with the highest temperatures occurring beneath the southern part of the field in excess of 325°C, suggesting renewed magmatic activity beneath the Coso region (Adams et al, 2000).

Geothermal production for electrical power generation began in the Coso geothermal field in the latter half of 1987 (Coso Operating Company, 2008). With no direct recharge of groundwater to the geothermal system, the Coso Operating Company began to pump water from the nearby Rose Valley groundwater basins for injection (Coso Operating Company, 2008). Geothermal wells reach down to depths of 3,300 to 10,000 feet into the system (Adams et al, 2000; Monastero, 2002). The fluid is flashed to steam allowing the steam to then power the turbine. The Coso Operating Company (2008) reports that the injection rate is approximately 50% of the production rate. This balance creates a loss of fluid within the reservoir that is continually being depleted each year causing the Coso Operating Company to seek other means of injection fluid from surrounding basins.

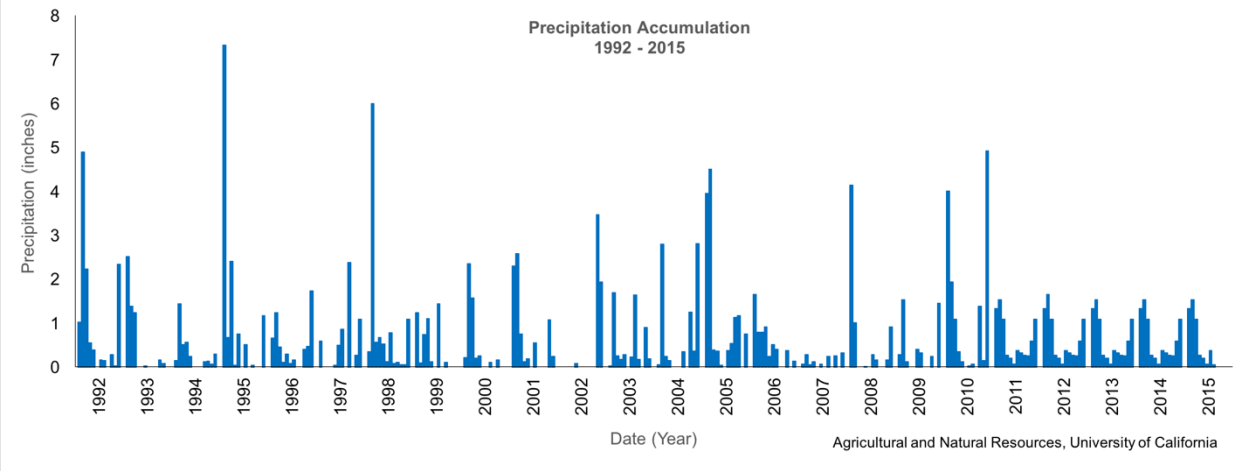

Figure 1.5: Precipitation summary 1992 to 2015. The precipitation values are representative to rainfall values experienced at Haiwee Reservoir, CA. Haiwee Reservoir is located on the NW extent of the Coso Volcanic field. On the X axis, data is ordered by month of progressing years throughout the years 1992 to April of 2015. The Y axis represents the experienced rainfall in inches. Data courtesy of (UofCal, 2014).

The loss of fluid has created a decrease in pressure within the system (Coso Operating Company, 2008). The large changes within the system over a 20-year period of production practices create a suitable situation for widespread surface deformation throughout the geothermal field. The continued contribution to instability within the system could also serve as a likely contribution to increases in seismicity occurrences above the assumed background seismicity expected within a tectonically active geothermal area. Feng and Lees (1998) supported this association with the spatial association of seismicity within the geothermal area to boreholes used for geothermal production.

1.8 Previous InSAR Work

Deformation trend analysis has previously been analyzed with differential interferometric synthetic aperture radar (DInSAR) techniques (Fialko and Simons, 2000; Wicks et al, 2001) throughout the Coso geothermal area in eastern California. This analysis used deformation observations as a tool to apply inversion calculations as a process to infer source depths of the driving mechanism for the Coso geothermal field. Wicks et al (2001) utilize this data to examine the implications of magmatic and geothermal processes occurring beneath the Coso Range. A region of high magmatic activity in present time and impacted by multiple eruptions within the previous 4 Ma. Fialko and Simons (2000) differentiates slightly in the focus of research where the impact of geothermal production processes is a primary concern. InSAR techniques are utilized to delineate areas affected by stress perturbations due to geothermal production. These areas support the understanding of possible causative links between the geothermal plant operation and observed seismic activity. The following section will review the methods of these studies and present significant results as they are relevant to this thesis.

Previous deformation analysis (Fialko and Simons, 2000; Wicks et al, 2001) in the Coso geothermal area has been performed and documented. This analysis covers trends throughout the years 1992-1998. SAR imagery covering the study period analysis was acquired from the European Space Agency (ESA) satellite missions of ERS-1/-2. Fialko and Simons (2000), utilized SAR imagery from 1992 through 1997, while Wicks et al (2001) focused on a slight temporal shift from years 1993 through 1998. The imagery covers a region approximately 50 to 100 square km centered on the Coso basin where DInSAR techniques were employed in an effort to model temporal trends taking place in a large continuous area.

Formation of interferograms requires the cross-multiplication of at least two complex SAR images by the multiplication of each pixel in one SAR image by the complex conjugate of corresponding pixels on the second SAR image. A processed interferogram allows the ability to infer ground deformation from the difference in phase values found in each pixel, an attribute contained in a complex SAR image as a result of SAR imaging processes. A more complete introduction to InSAR techniques is presented in section 2, showing the multiple steps that are required in the processing for InSAR analysis.

After formation, the removal of multiple phase contributions must be performed to provide an output modeling solely the phase difference ($\Delta\phi$), or ground deformation over time. In the studies of Fialko and Simons (2000) and Wicks et al (2001), interferograms were formed using a two-pass method. This entails that just two SAR images separated temporally are required for the formation of an interferometric pair. Topographic corrections are then applied using a previously established Digital Elevation Model (DEM), widely available from USGS sources. The phase values on an interferogram are a statistical quantity uniformly distributed over the interval $(0,2\pi)$ therefore a process known as unwrapping must be applied for a direct

measurement of surface change. Wicks et al (2001) applied this process using a branch-cut method (Goldstein et al, 1988). Examples of unwrapped interferograms can be found in Figure 3.2.2. Wicks et al (2001) built a period of analysis by establishing a series of five interferograms from scenes spanning twenty-four months between acquisitions. Atmospheric noise is an additional phase contribution that must be accounted for. This can be distinguished by analyzing signal persistence over several consecutive interferograms or several simultaneous interferograms spanning approximately the same time interval (Fialko and Simons, 2000).

Source modeling techniques present the ability to model relating ground surface deformations previously inferred from InSAR processes to volume changes at depth. Previous research (Fialko and Simons, 2000; Wicks et al, 2001) has employed multiple models of this analysis to the Coso geothermal area. The simplest model relating this occurrence is an isotropic point pressure source in a uniform elastic half-space (Mogi, 1958). Both studies determined that the deformation patterns throughout the Coso area is too complicated to be explained by such a model. To compensate for this, additional models were employed. Wicks et al (2001) employed one for a planar elastic dislocation (Okada, 1985), while Fialko and Simons (2000) incorporated a model using multiple prolate spheroidal sources (Yang et al, 1988). These models can be incorporated into a complex setting such as the Coso geothermal area by the addition of multiple model parameters such as movement perpendicular to the dislocation surface, and the strike and the dip of the planar surface as in the case of a planar dislocation source (Wicks et al, 2001).

Analyzing the calculated interferograms, deformation trends can be inferred for the study area. In this case, the inferred subsidence rate was found to be approximately 3 to 4 cm/year with an average volumetric subsidence rate of 10^6 m^3 per year (Wicks et al, 2001). The deformation included in these values was found to be distributed largely within broad subsidence patterns

surrounding the producing areas of the geothermal field. There are two localized subsidence peaks present in the area. One peak is located in the western while the other in the northeastern part of the anomaly that are separated by several km between. Fialko and Simons (2000) relate these trends to be likely results from the cooling and depletion patterns of the geothermal reservoir. Occurring in the later years of the study period, these large subsidence peaks in the western and northeastern regions seem to broaden and perhaps merge with time. Fialko and Simons (2000) suggest that this inferred broadening may reflect the deepening or perhaps lateral expansion of the deformation sources. Creating an increase in the reservoir volume that could be a direct effect of geothermal production. A significant find from deformation analysis is the presence of a dominant short and long wavelength. The short wavelength (~2 km) is found within the geothermal field that is assumed to be associated with the geothermal production and an area of active venting near coso hot springs. The long wavelength (~10-15 km) is a deeper source of deformation association, also indicating that this is a long-term reservoir drawdown (Wicks et al, 2001).

Source modeling that utilizes deformation trends from InSAR analysis allows the opportunity to model the source depths of the driving mechanism to the geothermal system in support of previous methods utilizing seismic data. Research in the Coso area has been focused around the determination for the heat source in the region. Reasenberg et al (1980) inferred that a body at depth was present from their research concluding low P wave velocity beneath the Coso geothermal area. Volcanic activity within the last 4 Ma supports the presence of a rhyolite magma body at depth contributing to two periods of eruption during this time. Previous analysis of long-wavelength deformation favors the presence of a source at range of 1-4 km depth (Fialko and Simons, 2000; Wicks et al, 2001). The structure of the heat flow impacting the geothermal

area is still in question. Wicks et al (2001) support the idea that the composite source is instead likely a shallow system of fractures driven by a magma body at greater depth and tectonic processes of the region. Source modeling from inversion calculations support the idea that this long-wavelength component of deformation is resultant from the thinning of the brittle rock above the magma body. This can create a scenario where breaches in the self-sealing zone allow movement of magmatic fluids upward into the region of circulating meteoric fluids creating the geothermal activity. The depressurization that occurs as a result to this breach of the brine-gas reservoir would then likely produce surface subsidence.

1.9 Contributions

The work assesses the patterns and magnitude of deformation at the Coso site from 2005 through 2010. Previous work in this region is temporally limited to the 1990s generated from the European Space Agency's (ESA) ERS-1/-2 satellite missions. This work employs a dataset that has not previously been considered from the ESA ENVISAT satellite mission. This ensures that the data utilized is from a different time period as well as generated from an independent sensor. Both flight modes are considered as a part of this work. Including both ascending and descending mode data assures the legitimacy of deformation patterns as data from independent flight modes are generated from different look directions. Results are consistent with the previous work of the Coso site for subsidence patterns and magnitude. The continuation of steady subsidence within the geothermal region suggest a linear deformation source over multiple decades.

1.10 Synopsis

Chapter 2 provides the technical background into the methods and understanding of

interferometric synthetic aperture radar (InSAR) analysis. Important SAR missions are presented with defining characteristics of missions utilized in this research. First, introduction of synthetic aperture radar (SAR) systems and SAR images are discussed. We then explain how these images can be paired accordingly to show deformation changes by the difference in phase lengths held in each image. We then describe how these calculated images can be used to model the temporal evolution of surface deformation for a region.

Chapter 3 presents the data that was utilized throughout the research process. SAR data implemented into interferogram generation and the satellite missions that provided the data are summarized. Earthquake datasets are used for interpretation of the impact that deformation has on the region from the Southern California Earthquake Center. DEM and additional GIS data that were utilized for analysis are presented. Additionally, the processing steps behind generating interferograms to infer the deformation trends and impact that surface change can have on the region as a whole are explained.

Chapter 4 presents the measured deformation rates exhibited at the Coso Geothermal site during the years 2005-2010 from differential InSAR analysis. Definition of potential trends that are discernible from the InSAR results. A discussion of the potential impacts or implications of these deformation trends are considered. As well as potential causes to the continued experience of these anomalies.

Chapter 5 discusses the future applications the can be implemented to improve or broaden the results that were presented as a part of this research. Some of these methods may consist of the implementation of additional SAR data from additional satellite missions of ERS-2 and Sentinel-1 that would broaden the range of years in the study period. Including the early 2000's and 2014 to the present. Additional steps may consist of the inclusion of additional

auxiliary data such as well data and the expansion of analysis with inverse modeling steps. Inverse modeling would allow a greater understanding towards the changes that have taken place in the subsurface during the study period.

Chapter 6 provides conclusions on the applicability of the analysis steps that were taken. As well as a summary of the results that were discovered as a result of the InSAR techniques. Concluding with a final look at what these results can mean to the impact of active production processes taking place in an active tectonic and natural geothermal region.

Chapter 2

InSAR for Crustal Deformation

Interferometric Synthetic Aperture Radar (InSAR) is an advanced remote sensing technique that utilizes the combination of two, or more, Synthetic Aperture Radar (SAR) images to create maps of an area that display terrain characteristics, such as topography and surface deformation, with a very high accuracy. Surface characteristics are expressed by the difference in phase values attributed to the radar-backscattered waves.

Radar technology has been utilized throughout the 20th century, with early practices consisting primarily of military intentions. Not until the early 1960s did side looking aperture radar become available to the scientific community from airborne sources. This followed the first experimental missions of spaceborne SAR, beginning in 1962 with the launch of Apollo 17. This Apollo Lunar Lander carried an L-band sounding radar to detect subsurface geologic structures, generate a continuous lunar profile, and map the lunar surface at radar wavelengths (Curlander and McDonough, 1991). Proceeding from the success of the lunar sounder mission and other airborne Jet Propulsion Laboratory tests, SAR found its first scientific utilization for Earth observation in the 1970s with the launch of Seasat in 1978 (Curlander and McDonough, 1991; Massonnet and Feigl, 1998).

The original purpose of the Seasat mission was the collection of data pertaining to sea surface characteristics (wave height, temperature, sea ice, and wind speed). The Seasat mission provided significant terrain data, along with sea surface data, to establish the validity of imaging for Earth observation using radar pulses aboard satellites. The success of the Seasat mission in turn led to the numerous Shuttle Imaging Radar missions, including SIR-A, SIR-B, and SIR-C. A

significant development in the SIR-B mission was a new antenna design that allowed images to be acquired at a varying degree of look angles from 15-60° (Curlander and McDonough, 1991).

The 1980s saw early published research for terrestrial applications of InSAR techniques (e.g., Zebker and Goldstein, 1986). The research of this time is significant from the lack of InSAR data availability that existed for scientific application. Following the ERS-1 satellite mission for spaceborne SAR in 1991, data availability increased significantly and allowed a more widespread inclusion of research teams abroad. Over time, more significant missions have taken place such as the ERS-2, ENVISAT, TerraSAR-X, COSMO-SkyMed, and most recent Sentinel-1 missions amongst others. The continuation of SAR missions suitable for InSAR techniques has resulted in an abundance of data suitable for geodetic analysis in many fields of research. Examples of these research areas include land subsidence (Aly et al, 2009), volcano development (Aly and Cochran, 2011), tectonics and earthquakes (Zhang et al, 2013), and geothermal environments (Sarychikhina et al, 2010).

2.1 Radar Basics

Radar (radio detection and ranging) instruments can detect features (Earth's surface) by emitting pulses of radio waves that are reflected off of surfaces (scatterers) and returned to be recorded (as backscatters) by the receiver of the radar system. These radar echoes can be used to infer the distance to the recorded scatterer and to generate a two-dimensional image of the area by measuring the two-way travel time (phase) from the antenna to the receiver. Radar imagery utilizes the microwave portion of the electromagnetic spectrum, which is approximately between 1 mm and 1 m wavelengths. Optical imagery systems have been widely utilized in remote sensing applications but contain some limitations to use as they are dependent upon day-time

light and require clear atmospheric conditions. Radar sensing systems have the advantage in these conditions as they have their own power sources and the microwave frequency allows radar waves to penetrate the cloud cover.

2.1.1 Real Aperture Radar (RAR)

RAR consists of a Side Looking Radar (SLR) with a fixed antenna length. The physically constricted antenna length creates a major limitation for RAR. The potential spatial resolution produced by RAR systems is typically too coarse (5-10 km) for use in surface analysis applications (Burgmann et al, 2000).

2.1.2 Synthetic Aperture Radar (SAR)

SAR systems possess a physically shorter antenna than that on RAR systems. SAR systems create a more precise resolution by synthesizing very long antennas through modified data recording and signal processing techniques. The SAR system follows the azimuth direction and continuously sends radar pulses across-track at designated time intervals. This results in the receiver sensing scatterers in consecutive echoes. SAR methods can distinguish the position of individual scatterers on the surface using the Doppler Effect from the relative motion of the antenna and the ground (Bamler and Hartl, 1998). In comparison to RAR systems, SAR spatial resolutions can be within a range of 4-30 m (Burgmann et al, 2000), providing a reasonable resolution appropriate for analyzing land surface changes.

2.1.3 SAR Imaging

The geometry of a spaceborne SAR system with a radar sensor mounted on a satellite at

height H is illustrated in Figure 1. The satellite travels along the orbit path (azimuth direction) at a designated velocity. With a side looking fashion, the system illuminates an area known as the antenna footprint on the Earth's surface through a series of microwave pulses. The radar pulses are emitted toward the target along the slant range, also known as the Line-Of-Sight (LOS) direction. Pulses reflect off of scatterers within the illuminated antenna footprint where the radar echoes return to the SAR system receiver. This process continues along-track emitting and receiving radar echoes forming a continuous strip-map of data.

Received radar echoes are summed to create a two-dimensional surface known as a complex SAR image. Recorded data within this image is in the form of a continuous pixel grid. The image is considered complex from the inclusion of attribute values within each pixel known as phase and amplitude (Feretti et al, 2007). Phase values represent the two-way propagation of the radar echoes, or the period of time that elapsed between emitting and receiving the radar signal. The amplitude, or the brightness of pixels, represents the intensity of backscattered energy off of scatterers on the surface. Usually, hard surface features such as urban areas and rocks will show a higher value of amplitude compared to surfaces such as water that will backscatter little energy returned to the receiver (Feretti et al, 2007).

Radar wavelengths typically utilized in common SAR systems are approximately 3 cm (X-band), 6 cm (C-band), and/or 24 cm (L-band). Most commonly associated with deformation analysis, are C-band wavelengths due partly to the abundant distribution of C-band data from the European Space Agency (ESA) satellite missions (e.g., the European Remote-Sensing satellites, ERS-1/ERS-2, and the Environmental Satellite, ENVISAT, Table 1). The variations of wavelengths create advantages for utilization in different geographical and land cover environments. Finer wavelengths (X-band) provide a higher precision for surface movement

detection commonly utilized in sparsely vegetated regions. Finer wavelengths have the disadvantage that the radar signals have a high possibility of being reflected off of vegetated features not representative of the surface. As the wavelength increases (C-band/L-band) the signal gains the ability to by-pass such features and capture the surface scatterers despite the land cover above. An additional advantage exists as a shorter wavelength has the capability to detect smaller surface movements in the Z axis. Detection of very gradual deformation within a region would benefit from this finer frequency and greater accuracy to small measurements over a larger period of time. On the other hand, larger wavelengths (C-band/L-band) accommodate faster rates of motion, as the rate of deformation will not exceed the length of a single radar wavelength.

2.1.4 SAR Data and Sensors

ESA has launched multiple satellite missions suitable for InSAR applications. Beginning in the early 1990s, the ERS-1 mission was the first ESA program in Earth observation. It was launched on July 17, 1991 and lasted until March 10, 2000. Its objective was to provide environmental monitoring in the microwave spectrum (ERS-1) with a 35 day mapping orbit. A detailed breakdown for significant parameters of each selected SAR mission is summarized in Table 2.1.

The ERS-1 satellite carried an Active Microwave Instrument (AMI). This sensor contains a SAR system that operates in two modes known as “Image Mode” and “Wave Mode”. The imaging mode operated at a C-band wavelength of 5.66 cm, and the wave mode served as a function to measure changes in radar reflectivity of the sea currents due to surface waves. The ERS-1 mission had multiple highlights throughout its lifespan. The benefits of this mission

served as a demonstration of range precision of 1 cm and the ability to detect small changes on the Earth's surface. This led to a significant increase within the scientific community of adaptation for SAR data within research of terrestrial applications.

The ERS-1 mission was followed by another ESA mission on April 21, 1995. This was the launch of a similar satellite known as ERS-2, until its retirement on September 5, 2011. The ERS-2 satellite was a base copy of the ERS-1 and contained the same mission objectives. The difference was that ERS-2 underwent some enhancements of sensor additions for improved vegetation analysis and the ability to measure chemical composition of the atmosphere. For SAR acquisitions, ERS-2 contained the similar AMI sensor operating at a C-band wavelength. One of the largest highlights during the lifespan of ERS-2 was its tandem mode with ERS-1 from July 1995 to July 1996. During this period the satellites collected precise topographic information as a result from the short temporal baseline between the two satellites.

A continuation of C-band data acquisition progressed with the launch of the ENVISAT satellite on March 1, 2002 until its end on May 9, 2012. The satellite followed a similar mapping orbital cycle of 35 days to its predecessors of ERS-1/-2. ENVISAT carried a sensor complement of Advanced SAR (ASAR), which is of similar development of the AMI sensors flown on ERS-1/-2. Significant new advances with ASAR consist of a flexible swath positioning, dual polarization, and wide swath coverage of 405 km swaths.

On June 15, 2007 the satellite mission TerraSAR-X was launched and managed by the German Aerospace Center (DLR). The intention of this mission is to make multi-mode and high-resolution X-band data widely available for scientific applications in a variety of fields (TSX (TerraSAR-X) Mission). The sensor complement onboard TerraSAR-X for SAR imagery is the TSX-SAR, which is an active phased array X-band system (TSX).

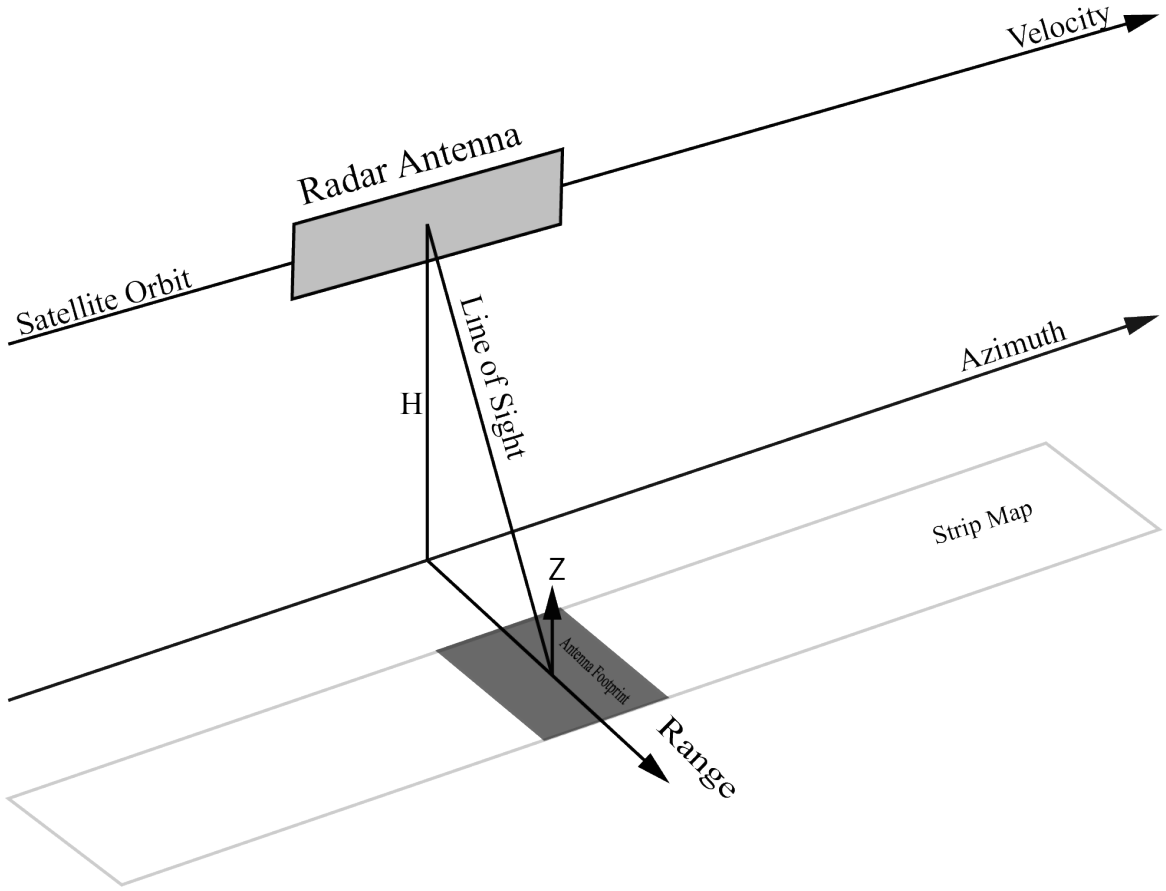

Figure 2.1: Synthetic Aperture Radar satellite terminology. The gray box represents the SAR system following the orbit path that travels at a designated velocity. The Line-Of-Sight (LOS) also known as the Slant range represents the path emitted radar pulses to and from the satellite. The Azimuth direction is also known as the along track, which represents the imaging path along the path of the satellite orbit. The range dimension represents the across track and the Z dimension represents the elevation of the surface. The antenna footprint represents the illuminated area of the radar echoes and the strip map represents the continuous imaged swath that is recorded along track (Ferretti et al, 2007).

Parameters	ERS-1 (Image Mode)	ERS-2 (Image Mode)	ENVISAT (Image Mode)	TerraSAR-X (Strip-map Mode)	Sentinel-1 (Strip-map Mode)
Launch date	7/17/1991	4/21/1995	3/1/2002	6/15/2007	4/3/2014
Termination date	3/10/2000	9/5/2011	5/9/2012	On-going	On-going
Orbit elevation (km)	785	785	800	514.8	693
Orbit interval time (days)	35	35	35	11	12
Inclination	98.52°	98.52°	98.52°	97.44°	98.18°
Antenna length (m)	10 x 1	10 x 1	10 x 1.3	4.8	12.3 x 1.02
Sensor complement	AMI	AMI	A SAR	TSX-SAR	C-SAR
Frequency (GHz)	5.3	5.3	5.3	9.65	5.4
Wavelength (cm)	5.66 (C-band)	5.66 (C-band)	5.66 (C-band)	3.1 (X-band)	5.5 (C-band)
Pulse bandwidth (MHz)	15.55	15.55	16	150	0 - 100
Pulse repetition frequency (Hz)	1640-1720	1640-1720	1650 to 2100	2000-6500	1000–3000
Pulse length (μs)	37.1	37.1	20	2 - 60	5 - 100
Sampling frequency (MHz)	18.96	18.96	19.2	10	260
Incidence angle	23°	23°	15 - 45°	15 - 60°	20 - 45°
Swath width (km)	100	100	100	30 (single) 15 (double)	80
Polarization	LV (linear vertical)	LV (linear vertical)	VV, HH, VV/HH, HV/HH, VH/VV	HH, VV, HV, VH (single or dual)	Dual HH+HV, VV+VH
Ground range resolution (m)	28	28	28	1.7 - 3.5	5
Slant range resolution (m)	10	10	8	1.2	1.7
Azimuth resolution (m)	5	5	5	3.3	5
One look range pixel size (m)	20	20	20	2	5
One look azimuth pixel size (m)	4	4	4	2	5
Ground coverage of one scene (km)	100x100	100x100	100x100	30x50	80x80

Table 2.1: Important parameters of selected SAR missions to demonstrate development of sensor technology over time.

One of the most recent launches of the ESA occurred on April 3, 2014. This was the launch of Sentinel-1. The objectives of Sentinel-1 primarily consist of the continuation of C-band SAR data availability. With that is the enhancement of data with the decrease of the mapping orbit to a 12-day cycle. The sensor complement onboard the Sentinel-1 is the C-SAR instrument. This component has four observation modes including the Stripmap mode for continued C-band imaging and an Interferometric Wide Swath (IWS) mode. The IWS mode has been given a new type of ScanSAR mode called Terrain Observation with Progressive Scan (TOPSAR) that is an attempt to reduce the disadvantages of the ScanSAR mode (Copernicus: Sentinel-1 – the SAR imaging constellation for land and ocean services). This new mode aims to produce the same coverage and resolution of past imagery from the ScanSAR, but with the advantage of nearly uniform Signal to Noise Ratio (SNR) and Distributed Target Ambiguity Ratio (DTAR).

2.1.5 Complications of SAR Imaging

Despite distinct advantages of SAR imageries, there are complications that need to be overcome throughout the imaging process in order to produce high quality images suitable for quantitative and qualitative analyses. These complications come from such aspects as land cover changes within ground pixels and topographic variations that cause LOS issues for the emitted radar pulses reaching the surface. Such complications and common practices employed to overcome them are discussed below.

1. Speckle:

Speckle is a complication that arises when several scatterers are within a single SAR resolution cell, then the amplitude values within the resolution cell fluctuate. This causes the

effect of speckle, which results in a grainy appearance throughout raw radar images. Use of multiple images covering the same region at slightly different times or look angles to average the values can greatly reduce this effect (Feretti et al, 2007; Bamler and Hartl, 1998).

2. Foreshortening:

Varying resolution cell sizes is greatly impacted by the slope of terrains in the across-track direction. The slope angle in respect to the LOS (look angle) is the deciding factor in this process. Foreshortening occurs as the slope of the terrain increases toward the radar system as seen on the side of a mountain. As the slope angle increases the radar is reflected from the bottom of the slope before the top. This compression creates a shortening effect and a misinterpretation of the true surface slope. The low incidence angle as a result of this situation provides a higher intensity and a brighter representation of amplitude in the complex SAR image (Feretti et al, 2007; Burgmann et al, 2000).

3. Lay-over:

Lay-over is another occurrence of slope representation found at extreme slope angles (top of mountain) where the slope of the feature exceeds the look angle. In this situation, the top of the feature is reflected before the bottom of the slope. This causes a layover effect for the displacement of the top of the feature over the base (Feretti et al, 2007; Burgmann et al, 2000).

4. Shadowing:

A shadowing effect occurs as the slope angle exceeds the minimum slope extent (0°). This creates a loss of surface representation as the feature slopes away from the radar sensor.

This occurrence is commonly found on the backside of topographic features in the across-track direction (Feretti et al, 2007; Burgmann et al, 2000).

2.2 SAR Interferometry (InSAR)

InSAR is a state-of-the-art remote sensing technique that can be used to derive surface information using two or more complex SAR images. Surface information that would otherwise be unattainable from a single SAR image. InSAR imaging techniques can produce data suitable for differing areas of research by varying the imaging methods that are used to represent the land surface. Along-track interferometry images the land surface parallel to its flight path, across-track interferometry images the land surface perpendicular to its flight path, and repeat-pass interferometry utilizes imaging of the land surface separated by designated periods of time to model long term surface changes.

1. Along-track Interferometry:

It utilizes two SAR antennas that are parallel to the flight direction. Each antenna emits and receives radar signals covering the same illuminated area in a single pass. The time delay between the two acquisitions is determined by the velocity of the system, which results in values typically within milliseconds of each other. Analysis of ocean currents and velocities (Romeiser and Thompson, 2000) is one of the main applications of the along-track interferometry. The analysis of rapidly changing scatterers is suited in this form of analysis by having the antennas separated in the along-track direction. This creates a very sensitive measure of the LOS velocity.

2. Across-track Interferometry:

It utilizes two SAR antennas that are placed perpendicular to the flight direction. Unlike the along-track interferometry, in the across-track interferometry only one antenna is used to transmit the radar signals. The backscattered signals are then received by the two antennas simultaneously in a single pass. The process of across-track interferometry is applied to the practice of topographic mapping (Bamler and Hartl, 1998). Significant data accumulation utilizing the across-track interferometry was applied to the Shuttle Radar Topography Mission (SRTM) (Farr and Kobrick, 2000). The SRTM mission concluded in February of 2000 and resulted in the accumulation of digital elevation data of 30-m spatial resolution for the USA and Canada and of 90-m spatial resolution for the rest of the world.

3. Repeat-pass Interferometry:

Differential InSAR utilizes SAR images of temporal separation that ranges from one day to numerous years. Acquisition of InSAR data comes from imaging the same region by a single antenna with relatively the same viewing geometry. The temporal separation creates an advantage of monitoring of geophysical change. Repeat-pass interferometry has been applied to such research fields as volcanic activities (Hooper et al, 2007; Aly and Cochran, 2011), land subsidence (Hole et al, 2007; Aly et al, 2009 and 2012), seismic occurrences (Fialko and Simons 2001), and glacier dynamics (Wangensteen et al, 2005).

Illustrated in Figure 2 is the repeat-pass interferometry method. The separation between the satellites along-track is called the baseline (B). The baseline perpendicular to the orbit is called the interferometer baseline and the baseline perpendicular to the slant range is the perpendicular baseline. This serves as a factor in decorrelation effects discussed later. At time period t1, the radar pulses reflect ground pixel I_1. The received echo provides a measurement of

phase value ϕ1. The second pass by the SAR satellite at time period t2, repeats this process for the same area at ground pixel I_2. This again provides a measurement of phase value ϕ2. If scatterers within the ground pixel have changed minimally in the lapse of time, then they will contribute to ϕ2 the same as they had for ϕ1. Phase values from each pass provide the measurements to calculate the phase change (I) over the designated period of time between radar echoes.

2.2.1 Interferogram Generation

Interferometric processing begins with the acquisition of either raw data or Single Look Complex (SLC) images. Raw data contains signal information of the object of azimuth and range bandwidth. Raw data must undergo a series of processing steps before it is suitable for SAR interferometry processing. SLC images contain positional information as well as the phase and amplitude information from the SAR data. When two or more SAR images are acquired the second image must first be coregistered and resampled to the geometry of the first image. Coregistration requires precise association within sub-pixel accuracy of ~0.1 pixel.

To form an interferogram, the images are then cross-multiplied for each pixel in the first image by the complex conjugate of corresponding pixels on the second image. Ignoring errors in the imaging hardware, the interferometric phase (Δϕ) can represent the difference in path length to a designated scatterer from the imaging system to the target along the LOS direction. The interferogram is produced as follows (Hellwich, 1999):

$$\mathrm{I} = I_1 I_2^* = A_1 A_2 \bullet e^{i(\phi_1 - \phi_2)} \qquad (1)$$

where, I_1 is the amplitude and phase of image 1, and I_2 is the amplitude and phase of image 2, and * indicates the complex conjugate of image 2, and $\phi_1 - \phi_2$ represents the interferometric phase.

Surface deformation studies require the removal of the topographic phase contribution. This is estimated and removed by using a DEM created from InSAR processing techniques or by using an existing DEM generated from digital elevation data acquired by other missions such as the Shuttle Radar Topography Mission (SRTM). DEM accuracy is a vital factor of this step. DEM errors can result in direct translation to phase errors within the interferogram. Additionally, urban areas can create a difficulty from the elevation amongst structures. DEMs reflect the ground elevation, while the radar values of a SAR image will likely record the elevation of the building surfaces, creating a difference in elevation values. The topographic phase can be estimated as the following:

$$\phi_{topo} = \frac{4\pi\beta z}{\lambda\rho sin\theta} \quad (2)$$

where, ϕ_{topo} is the topographic phase, β is the perpendicular baseline between the imaging SAR antennas, z is the height of the topography recorded, λ is the radar wavelength, ρ is the range, and θ is the look angle of the sensor.

2.2.2 Phase Unwrapping

Phase values represented in the raw interferogram are measured in the interval (0, 2π). This requires the need for conversion of the cyclic phase values to continuous absolute values. This

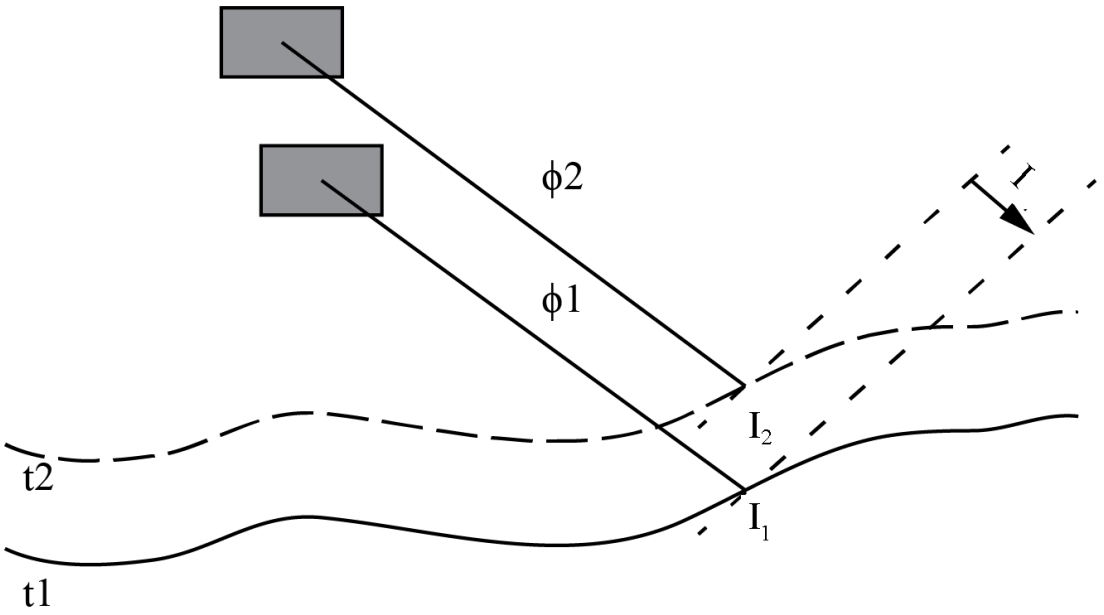

Figure 2.2: InSAR imaging geometry. At first time designation t1, point I_1 is the designated target location. Radar pulses are emitted along the LOS and phase ϕ1 is measured. At an extended period of time following t1, ground at t2 reflects another radar pulse at ground pixel I_2. The Z dimension of ground is measured by phase ϕ2. The phase difference I, is calculated utilizing equation (1) (Bamler and Hartl, 1998).

process of adding the correct integer multiple of 2π to the fringes is called phase unwrapping (Burgmann et al, 2000). Multiple phase unwrapping algorithms are discussed in Bamler and Hartl (1998). These consist of the least squares (Bamler and Hartl, 1998), branch-cut (Goldstein et al. 1988) and minimum cost flow methods (Constantini, 1998), among additional methods that have been applied in numerous studies. Following phase unwrapping, a geocoding step is traditionally implemented to project the interferometric data to a common reference system. This creates a more universal data platform to be combined with data from other sources.

2.2.3 Phase Decorrelation and InSAR Limitations

The unwrapped interferometric phase consists primarily of five phase contributions (Aly et al, 2009):

$$\Delta\phi = \phi_{def} + \phi_{topo} + \phi_{orb} + \phi_{atm} + \phi_{noise} \quad (3)$$

where, ϕ_{def} refers to the phase due to ground deformation, ϕ_{topo} refers to the phase due to topographic contributions, ϕ_{orb} refers to the orbital phase error, ϕ_{atm} refers to phase delay caused by atmospheric artifacts, and ϕ_{noise} refers to the system phase noise.

A quality assessment of InSAR data is the coherency between SAR acquisitions. Coherency results in a value between 0 and 1 (1 representing perfect phase correlation between both image pixels and 0 representing no correlation between coinciding image pixels). InSAR coherence can be affected by decorrelation between the image pairs.

Phase decorrelation arises as a result of spatial and temporal changes. Spatial decorrelation occurs as the spatial separation between the SAR systems exceeds the critical

baseline. Temporal decorrelation occurs as the surface changes throughout time. Regions that undergo seasonal transitions can cause decorrelation as the growth and loss of vegetation results in no coherence. Seasonal transitions can consist of snowfall throughout the winter that will inhibit coherency differences as it is not present in the warm months. Estimation of phase noise is determined by the local coherence of the interferometric pair (Feretti et al, 2007). Local coherence is estimated by a cross-correlation coefficient between corresponding pixels of the interferometric pair contained within a small moving window. The coherence map is then formed as a result of the absolute value of coherence (Feretti et al, 2007). Phase noise reduction can be performed prior to phase unwrapping to ensure the success and accuracy of the unwrapping process. It can be achieved by applying a filter to the interferogram such as a moving-average filter or a non-linear adaptive filter (e.g., Goldstein and Werner, 1998).

The interferometric phase measurement can be greatly affected by the accurate knowledge of the relative position of the two SAR system orbits. A priori knowledge of the orbital information is used to eliminate the inaccurate contribution of fringes. The interferometric effect can also be depleted if the images shift by more than a half a wavelength in corresponding pixels (Massonnet and Feigl, 1998). An inaccurate estimate of the perpendicular baseline will cause bias within the elevation estimate, and thus the deformation contribution will be inaccurate as a result of the wrong estimation of elevation.

Despite the advantage of radar systems being able to image in all weather conditions, a medium, such as the atmosphere can still modify the propagation of electromagnetic waves by the changes within the refractive index. This will create a change within the travel time measured by the radar system. If the acquisition times have any temporal separation, then the interferomteric phase will be affected by the atmospheric artifacts. These errors can generally be

eliminated by applying a sequence of spatial and temporal filtering to preserve phase trends in a time series (e.g., Aly et al, 2009). Interferogram stacking can also reduce the effects of atmospheric contributions. More advanced quantitative methods use atmospheric data acquired simultaneously by other sensors mounted onboard of the radar platform.

2.2.4 InSAR for Topographic Mapping

Output of topographic analysis utilizing InSAR techniques constitutes the generation of an interferometric DEM. InSAR serves as a reliable technique for modeling the Earth's surface topography as the accuracy within tens of meters results in a high quality DEM output. SAR imaging processes also eliminate the restriction of optimal weather as radar imaging can be taken under any weather conditions during day and night.

SAR images as a result of across-track interferometry and repeat-pass interferometry are utilized for DEM generation where the spatial baseline difference is present to create a slightly different viewing angle. Following interferogram generation and phase unwrapping techniques previously discussed, the topographic contribution to the phase is isolated to give the topographic values of locations within the interferogram, and then a phase to height conversion is conducted.

$$h = p\ \sin\left(\cos^{-1}\left(\frac{\phi\lambda}{2\pi\beta} - \theta\right)\right) \qquad (4)$$

The vertical distance to the SAR antenna is determined with the along-track distance in order to determine the 3-dimensional location of each point in space (Zebker and Goldstein, 1986) with the use of equation 4. This provides the topographic measurements within the region.

The image must then be transformed to geographic coordinates in a square grid by the following:

$$y = (p^2 - h^2)^{1/2} \quad (5)$$

Topographic mapping utilizing InSAR techniques can be applied to many settings with world coverage provided by SAR imagery missions. Rossi et al (2012) tested the applicability and functionality for DEM generation provided by the tandem mission of X-band radar known as TanDEM-X (Figure 3). This mission consisted of a tandem operation between the DLR satellite missions TDX and TerraSAR-X. The DEM generation methods were applied to the Cordillera Central Mountains in Peru. Results of the DEM applicability by Rossi et al (2012) suggest a mean coherence for the DEM of 0.65 and a mean height error of elevation values within the DEM of 2.76 m.

2.3 Common InSAR Processing

2.3.1 Conventional InSAR Techniques

Two-pass InSAR

Two-pass interferometry is a method that is accomplished by using two SAR images accompanied by an external DEM for the corresponding area. After calculation of the interferogram, the topographic contribution is then removed using the existing DEM. This removes unwanted fringes, while the signal of interest is left behind (Massonnet and Feigl, 1998). The advantages of the two-pass method are a result of simplification and preservation of time

and effort. Minimal images are required to formulate an interferogram and there is no need for a topographic interferogram. The major disadvantage of this method is associated with the quality assumption of a previously formulated DEM. Unknown errors can exist within the DEM which result in errors within the interferogram.

Three-pass InSAR

Three-pass interferometry is another form of conventional InSAR that requires only the acquisition of three SAR images for the analysis. No external elevation data is required as two of the SAR images are used to construct a topographic interferogram that can be used for the topographic correction. Then, one of the SAR images used for the DEM creation is combined with a third SAR image for the formulation of an interferogram that contains topographic and surface deformation contributions. The extra processing steps for the unwrapping of the topographic interferogram is a disadvantage of this method. The unlikelihood of finding three radar images that are mutually coherent is the main disadvantage of 3-pass InSAR.

Four-pass InSAR

The four-pass InSAR method uses a similar process as the three-pass method but requires the association of four SAR images taken at different times. Two of the images are associated to create a topographic interferogram while the other two unused images are associated to create an interferogram that contains topographic and deformation contributions.

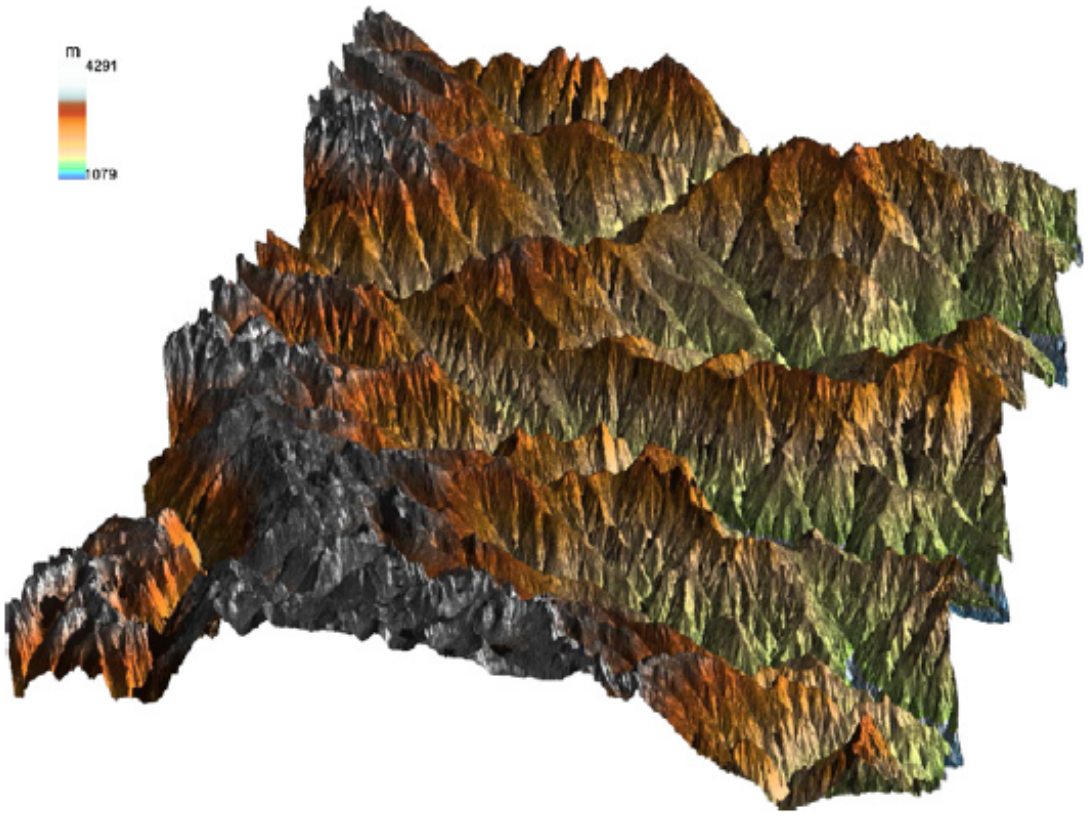

Figure 2.3: Hill-shaded relief generated from DEM data as a result of the TanDEM-X mission by Rossi et al (2012). Elevation heights illustrated by color ramp in upper left corner (Rossi et al, 2012).

2.3.2 Advanced InSAR Techniques

Persistent Scatterer Interferometry

Feretti et al (2000; 2001) formulated an extension to conventional InSAR techniques called Permanent Scatterer InSAR to overcome decorrelation problems of conventional InSAR by using a pixel-by-pixel approach. Individual pixels are selected as dominant scatterers that exhibit coherence over significant periods of time. Examples of such scatterers consist of bare rocks and urban structures. Other similar approaches with some modifications called Persistent Scatterer InSAR (PSI) were introduced in the following years (e.g., Hooper et al, 2004; Hole et al, 2006; Hooper et al, 2007). These methods allow almost all archived SAR images, regardless of their perpendicular and temporal baselines, to be considered for PSI analysis by addressing problems with decorrelation and atmospheric inhomogeneity within the pixels of the created interferograms for a specific region.

Contributions to an individual pixel's variation of phase and amplitude values are a sum of individual wavelets reflected by multiple scatterers within the resolution cell. The amount of decorrelation within the cell is determined by this balance of constructive and destructive contributions of wavelets. Complete temporal decorrelation occurs as scatters within the contributing pixel are not stable over time when they have move large distances during acquisition periods in comparison to their radar wavelength (Feretti et al,, 2001). In contrast, a PS pixel will entail the contribution of an individual scatterer much brighter than the others. This brighter scatterer likewise is the greatest contributor to the phase of the pixel. As the other scatterers move around, the pixel phase is relatively unchanged as the signal received is primarily controlled by the measurement of this PS (Feretti et al, 2001).

Small BAseline Subset (SBAS)

An additional extension to conventional InSAR methods is known as the Small BAseline Subset (SBAS) technique proposed by Berardino et al (2002). The aim of this technique is to minimize the spatial decorrelation and topographic errors that are experienced from traditional InSAR methods. This is accomplished by combining a large number of SAR images into a time series of interferograms that all contain a small spatial and temporal baseline as well as a small Doppler center frequency difference relative to each other (Liu et al, 2013). For a detailed explanation consult Berardino et al (2002). Similar to PSI, SBAS methods apply a pixel by pixel approach to high coherence areas within the intended region of study. This creates advantages of this method in the removal of possible errors of a DEM and the removal of atmospheric artifacts with the utilization of a space-time filtering operation (Berardino et al, 2002).

2.4 Solid Earth Applications

Active Volcanoes

Volcanic eruptions can pose a potential great threat to infrastructure and public safety. Even collapsed calderas that are deemed inactive can regain energy once more. Currently, all active volcanoes and volcanic centers are monitored by InSAR satellites. Aly and Cochran (2011) analyzed crustal deformation at Yellowstone between 1992 and 2009 utilizing various InSAR data acquired by ERS-1/-2 and ENVISAT satellites. Their investigation determined four distinct episodes of subsidence and uplift (Figure 4) during the study period. Episode 1 consisted of broad subsidence measuring approximately 2.7 cm/year, centered within the caldera throughout

1992-1995. Episode 2 consisted of a slower rate of regional subsidence measuring approximately 0.5 cm/year throughout 1996-2000. Episode 3 consisted of regional subsidence measuring approximately 0.7 cm/year throughout 2000-2004. Episode 4 consisted of regional uplift measuring approximately 3-8 cm/year throughout 2004-2009. They concluded that the magmatic and hydrothermal processes that are present beneath the Yellowstone caldera can be linked as the primary causes for the deformation occurrences and the major structural faults have no role to play as no differential displacements have occurred along any of these faults.

Earthquakes and Fault Interactions

The interplay between tectonic processes and earthquake occurrences can be modeled and studied with InSAR techniques. Zhang et al (2013) applied these methods to the 7.1 magnitude Yushu earthquake that occurred in 2010. They aimed to obtain a robust rupture process and slip distribution of the event. From the analysis they determined that InSAR analysis was even able to resolve better fault slip at near surface depths than teleseismic data (Figure 5).

Land Subsidence and Ground Stability

Ground subsidence can serve as an indicator of active tectonic or volcanic process or even indicate areas of significant subsurface fluid loss. The effects of subsidence can cause costly infrastructure damage yearly. Aly et al (2009) analyzed subsidence patterns within Cairo, the capital of Egypt. They applied Persistent Scatterer InSAR utilizing ERS-1 and ERS-2 data and measured an annual rate of subsidence throughout the area of approximately 7 mm between 1993 and 2000 (Figure 6).

Landslides and Mass Movements

InSAR can be utilized also in monitoring active and potential landslides. Hilley et al (2004) demonstrate this capability for the Berkeley vicinity in eastern San Francisco Bay area. The Permanent Scatterer technique was employed to demonstrate the increases of ground displacement with seasonal precipitation increases. To aid this assumption the El Nino event of 1997-1998 was captured within the study period of 1992 to 2001. Before and after the El Nino event, the displacement could not be detected, while during the El Nino event (November 1997 - April 1998) range-change rates increased by approximately 30% to maximum rates of 35 mm/yr (Hilley et al, 2004). They concluded that the association of landslide motion with high precipitation indicates that the near-surface groundwater flow does initiate and accelerate the association and rate of surface sliding in areas of slope increases.

Geothermal Processes

Areas of geothermal activity can pose a threat from significant subsidence and induced earthquake activity. Constant fluctuation of fluids within a geothermal system cause movement and create a potential scenario for increased seismicity. Sarychikhina et al (2010) analyzed the geothermal field in the Mexicali Valley in northwestern Mexico with Differential InSAR techniques. They employed ENVISAT data throughout the study period of October 2003 to March 2006. They determined an area of significant deformation approximately 10-16 cm/year (Figure 8).

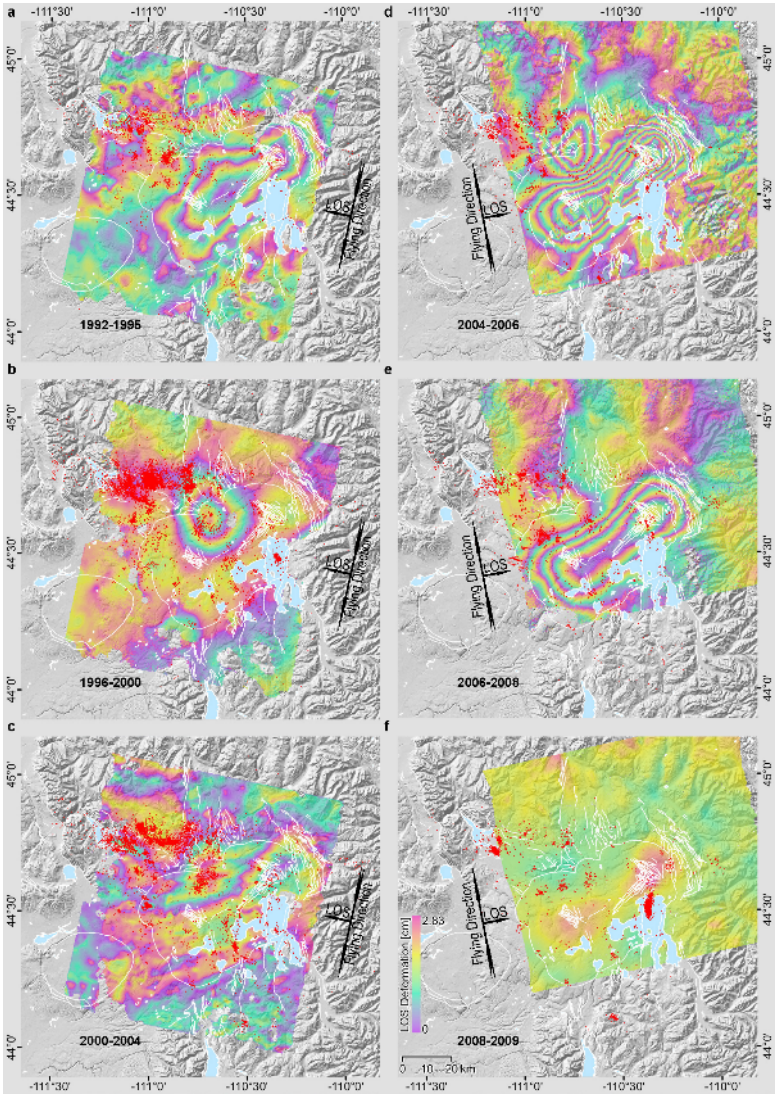

Figure 2.4: InSAR interferograms showing episodic inflation and deflation at Yellowstone (from Aly and Cochran, 2011). Images contain periods of deformation indicated by time designations in lower left of individual images. Each color fringe represents 2.83 cm of Earth's surface motion toward or away from the satellite (Aly and Cochran, 2011).

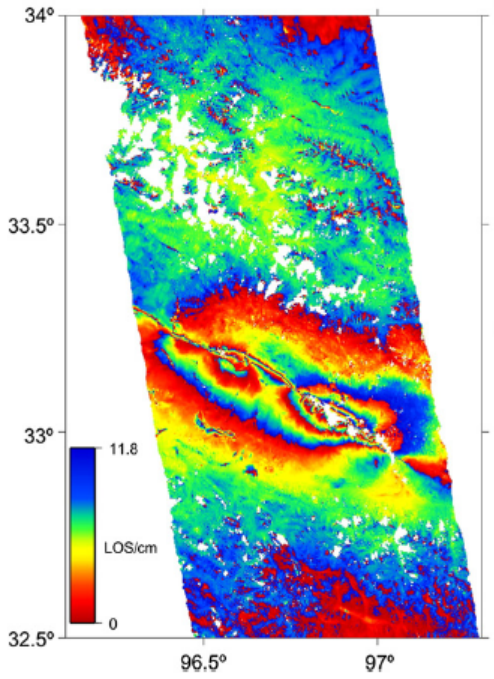

Figure 2.5: Coseismic deformation of the 2010 Yushu earthquake detected by InSAR from Zhang et al (2013). Peak deformation along the causative fault resulted in approximately 42 cm of motion on the south side and approximately 38 cm of motion along the north side (Zhang et al, 2013).

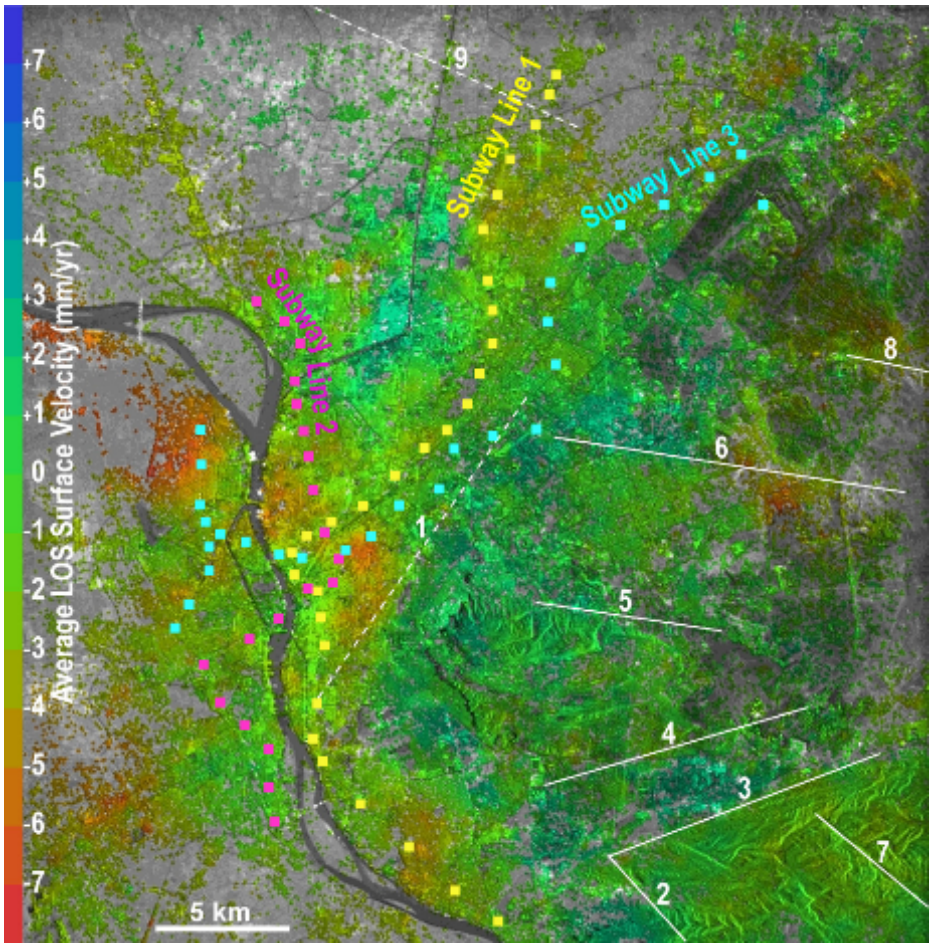

Figure 2.6: Average velocity of ground deformation in Cairo, Egypt, during 1993-2000 (from Aly et al, 2009). Mean LOS surface velocity is superimposed on the average amplitude image. Solid white lines represent major surface faults. Dotted white lines represent major subsurface faults. Deformation from InSAR is displayed with correlation to the color ramp (Aly et al, 2009).

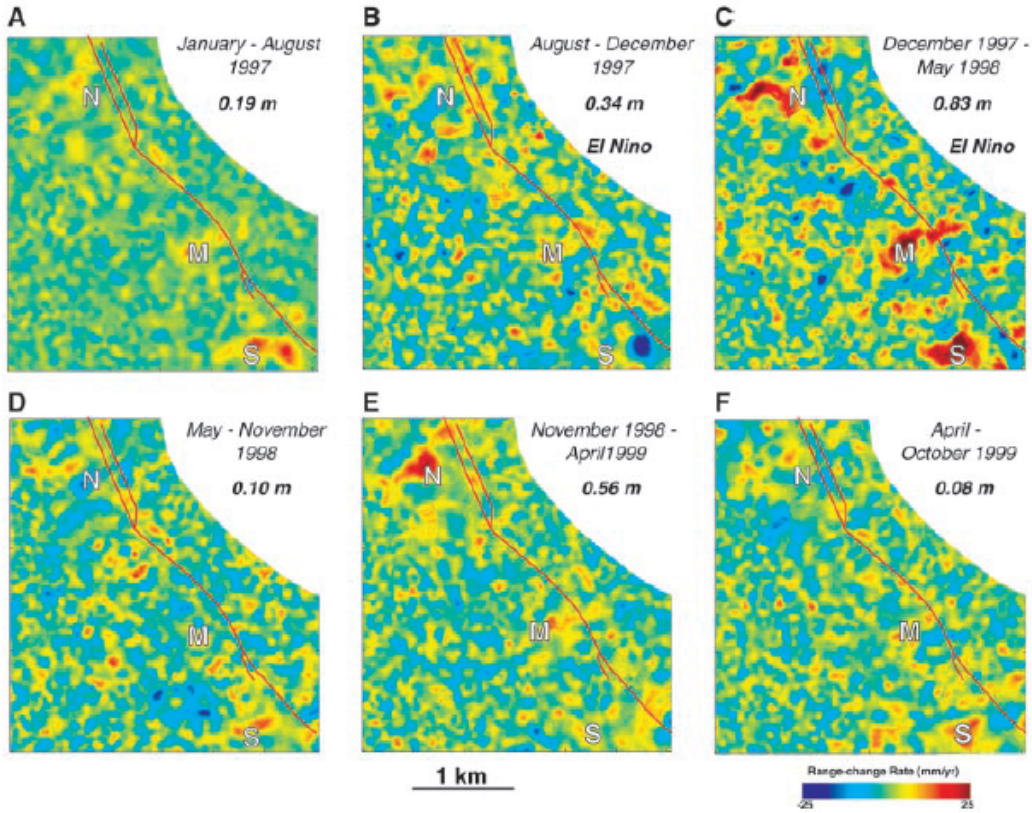

Figure 2.7: Range-change rates for the Berkeley vicinity in eastern San Francisco Bay area (from Hilley et al, 2004). Time periods indicated in upper right corner of individual images. Precipitation accumulation is indicated by bold numbers measured in meters (Hilley et al, 2004).

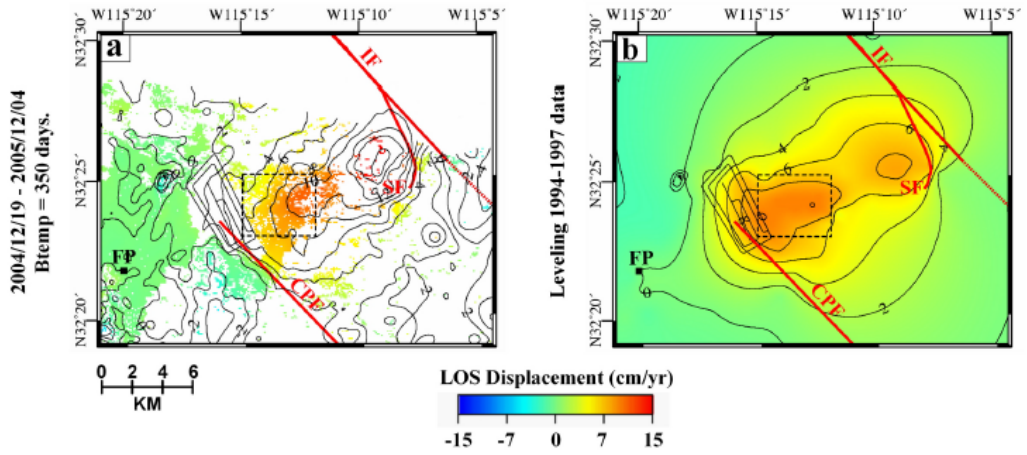

Figure 2.8: Surface displacements occurred at the geothermal field in the Mexicali Valley in northwestern Mexico (from Sarychikhina et al, 2010). (a) displays the displacement measured by stacking 4 differential interferograms from December 2004 to December 2005. (b) displays displacement rates obtained from a leveling survey during 1994-1997 (Sarychikhina et al, 2010).

2.5 Software for InSAR Processing

Various software packages can be utilized for InSAR analysis. Different software packages present a different aspect of applying the InSAR techniques to a desired study application. Preference of use for each package is predominantly selected based on the individual need in their specific area of research. Commercial level packages offer the most resources as far as applying to the intended field of study. Common packages in this category consist of GAMMA Remote sensing, SARscape, and DIAPASON. GAMMA is a Swiss corporation producing software for radar remote sensing applications including interferometry. It utilizes a command line operation in C language. SARscape is another commercial package for processing SAR images under the IDL scientific programming environment. In addition, the French Space Agency (CNES) produces a commercial software package known as DIAPASON with good processing capabilities for SAR images.

There is also a large accumulation of open source software packages for InSAR analysis. One of these packages is produced by the Jet Propulsion Laboratory named Repeat Orbit Interferometry Package (ROI_PAC). This package led to the production of the InSAR Scientific Computing Environment (ISCE). ISCE was produced to fit the specific needs of current and past spaceborne data as an update to ROI_PAC incorporating the recent SAR sensors. Other open source packages exist such as DORIS that is developed and maintained by the University of Netherlands, GMTSAR that is developed by the University of California in San Diego, and STAMPS that was produced originally at Stanford University. Matlab is the interface used in STAMPS.

Chapter 3

Data and Methods

The methods described within this chapter represent a process of skill development for InSAR and advanced remote sensing techniques. A large portion of the research process was spent as a skill development process towards understanding how to perform InSAR analysis. While understanding the intricate steps involved to complete an appropriate analysis utilizing these cutting edge remote sensing techniques to analyze a real world problem.

Additionally, this research serves as an analysis of modern deformation trends within the Coso Geothermal site. Deformation trends from 2005 to 2010 will be assessed to judge the stability or change in deformation rates from earlier analysis of the 1990's (Fialko and Simons, 2000; Wicks et al, 2001). The Coso region has been untouched in the assessment of deformation rates from the conclusion of these preceding studies. Modern analysis of these trends are necessary to determine the potential change or stability of deformation rates in the region as time continues to progress and geothermal production practices continue to operate at the site.

3.1 Data

Synthetic Aperture Radar (SAR) data utilized in this research was provided by the European Space Agency (ESA) satellite mission of ENVISAT. The ENVISAT satellite was launched on March 1, 2002. Imagery is available from this launch date until approximately May 9, 2012 coinciding with the mission's termination date. Individual images for a designated study sight can be retrieved every 35 days. A period of time that is associated with the satellite's orbit

interval rate.

The ENVISAT mission as discussed in Chapter 2 carried the sensor component ASAR (Advanced SAR) that measured radar backscatter at C-band wavelengths (5.66 cm). A C-band wavelength is appropriate for the study area located in southeastern California. This regions predominant land cover consists of high desert scrub. The lack of vegetative cover allows radar signals to reflect off of the true ground surface unimpeded. Imagery of high accuracy and high coherence can be acquired under these conditions.

The ASAR sensor was capable of imagery in multiple operating modes such as Wide Swath Mode, Wave Mode, Alternating/Cross Polarization and Image Mode. The appropriate imaging mode for this research is provided by the Image Mode. The Image Mode provides data accumulation over a predetermined swath (up to 100 km) in a total viewing area of 485 km and a spatial resolution of 30 m.

Data collected from the European Space Agency's ENVISAT mission consisted of a total of 21 images from Track 349 Frame 711 of the ascending mode with dates between March 03, 2006 to October 08, 2010. 31 images were also collected from Track 442 Frame 2289 of the descending mode with dates between October 16, 2003 to August 05, 2010. The term ascending mode corresponds to the predominantly South to North orbit direction of the satellite. During this pass the imagery is recorded in the across track direction pointed to the East as a result of the side looking fashion of the sensor. Likewise, the descending mode corresponds to the predominantly North to South orbit direction that captures imagery as the across track direction is pointed to the West.

Two-pass differential interferometry methods as applied in this research, require the use of two Synthetic Aperture Radar (SAR) images for calculation of the interferogram and the use

of a digital elevation model for the removal of the topographic contributions from the interferograms (as discussed in Chapter 2). Removal of the topography along with additional contributing factors allows the ability for deformation movements throughout the study period to be isolated and displayed in the form of interferograms. The DEM data utilized in this research are generated by the Jet Propulsion Laboratory (JPL) as a result of the Shuttle RADAR Topography Mission (SRTM). and archived at the United States Geological Survey (USGS) where the data is readily available for download.

Earthquake records can be utilized as an additional measuring device to the severity of impact that they region of deformation is having on local to regional processes and potential geohazards that may be a possibility as a result to the movement in the study area. Earthquake records were collected for the Coso region for each year of analysis represented by the interferograms (2005-2010). These records were collected from the Southern California Earthquake Data Center (SCEDC). The data is the archive of the California Seismic Network (CSN). The earthquake records compared to the deformation patterns can be viewed in Figures 4.2 to 4.15 Earthquake occurrences for the years of combined deformation analysis are displayed as an overlay on the record of deformation for the region. This allows the possibility of inferring any connections between the pattern of deformation and potential earthquake clustering. High clustering in the center of deformation can be a result of dominant ground movement.

3.2 InSAR Processing

SAR data in its raw format requires multiple processing steps before it can be utilized for InSAR analysis. This raw data is a collection of signal data that consists of amplitude and phase measurements. An accumulation of data that cannot be viewed as an image.

The first step is to transform the raw data to a format referred to as a Single Look Complex (SLC). SLC images retain the amplitude and phase values while correcting for satellite reception errors. The transformation to SLC images will also align the reflected values to their proper location within the study area. SLC images are stored in slant range geometry. This entails that the pixels are not traditional square pixels but ones that will increase as the slant range increases in the across track direction.

A process referred to as multi-look averaging can be applied to SLC images. This process combines adjacent looks to form a more consistent pixel size. These outputs form a displayable amplitude output of the study area as illustrated in Figure 3.1. The brightness values of each pixel displayed in this image represent the amplitude (or the strength of signal reflection to the sensor).

Two-pass differential interferometry was applied in this research. This requires the usage of two SLC images to calculate the resulting interferograms. Prior to interferogram calculation, SLC images must be compared to determine acceptable pairs for combination. This is determined primarily by two factors. First consisting of the perpendicular baseline. The perpendicular baseline is a measurement of difference between the satellites baseline perpendicular to the slant range. When comparing baselines, the smaller the value the more likely the SAR pair is to be combined with high coherence. Optimally, the value will be around 100 m or lower. The second factor is referred to as the temporal baseline. The temporal baseline is the separation of time in days between the orbits of each SAR image in the intended pair. Selected SAR pairs for interferogram calculation and inclusion in this research are presented in Tables 3.1 and 3.2. Tables are separated according to their association with the ascending and descending modes of data acquisition. Dates of the pairs as well as the perpendicular baseline

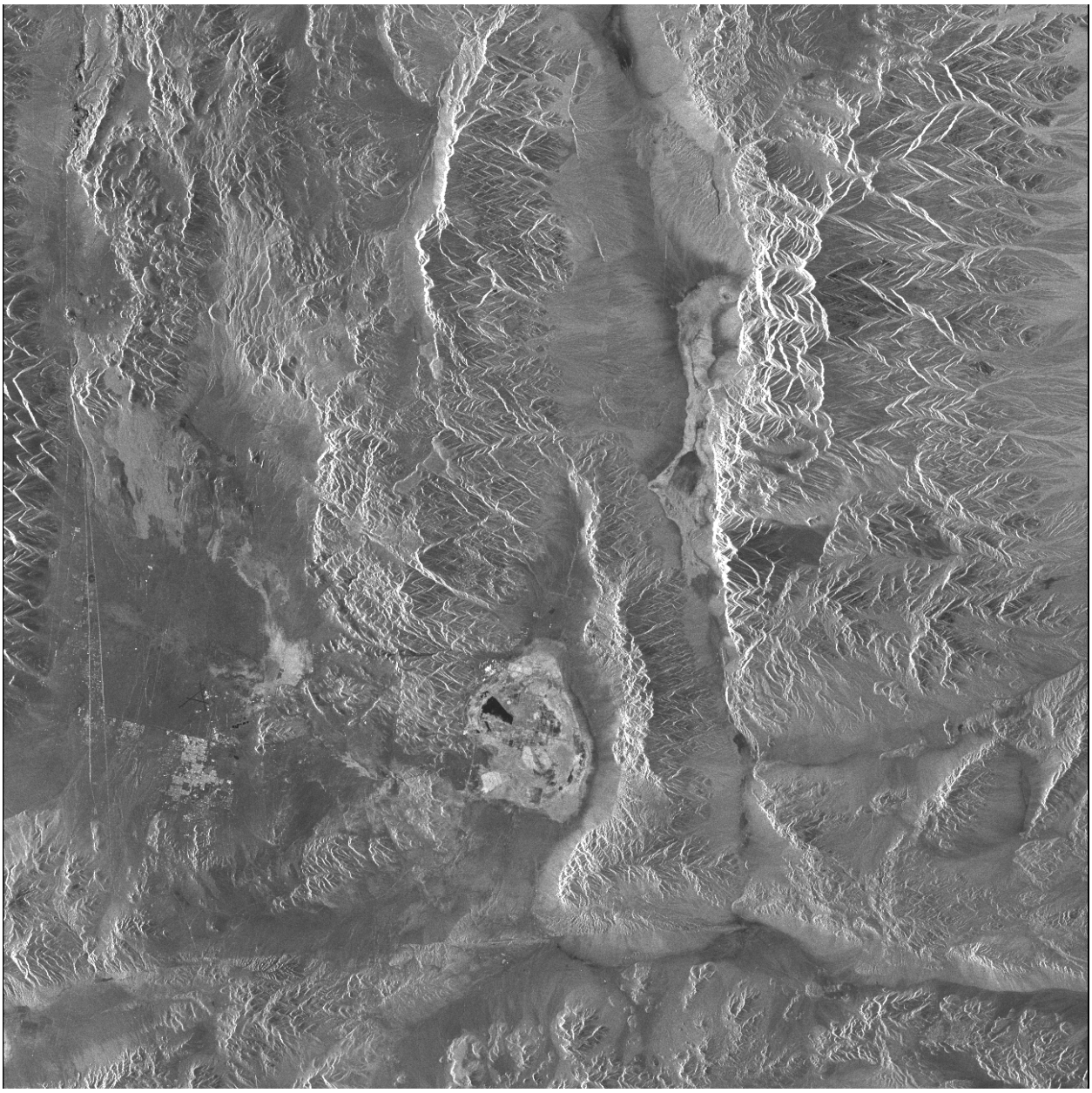

Figure 3.1: Amplitude image of the Coso region. Image is multi-looked to 4 looks in range and 20 looks in azimuth from a generated SLC image. Data acquired from ascending mode of the ENVISAT satellite mission.

and temporal baseline values are summarized as well.

Differential InSAR processing starts with the coregistration of the two SAR images from the selected pair. This step ensures that the pixels within the two selected images have been aligned to each other precisely within sub-pixel accuracy of -0.1. Precise alignment is necessary for the coherence of the resulting interferogram. Poor coherence will result in corresponding inaccurate surface movement measurements.

Properly coregistered SAR images can then be combined to form the initial interferogram. The process to calculate the interferogram involves the multiplication of each pixel to the complex conjugate of the corresponding pixel in the paired image. The resulting interferogram as discussed in Chapter 2 contains the real deformation experienced within the study area as well as multiple other contributions of which need to be removed. The removal of these additional contributions will isolate the real deformation that has taken place over the designated time period.

Two-pass differential interferometry also requires the usage of an existing digital elevation model for the removal of the topographic contribution. A Digital Elevation Model (DEM) can be acquired from the United States Geological Survey (USGS). This DEM must be a coverage that exceeds all extents of the SAR data in use. The DEM is clipped to the extent of the selected interferogram. The DEM must then be coregistered to the interferogram to ensure an accurate removal of the topographic contribution. A parameter file created in these steps is utilized for the forward and backward geocoding of the DEM and output interferogram later discussed.

Deformation patterns (values) are displayed on the initial interferogram as range change modulo 2π as the radar signal reflects from the ground back to the satellite sensor. Fringes are

Master Date	Master Orbit	Slave Date	Slave Orbit	Perpendicular Baseline (m)	Δt (days)
20060303	20944	20070112	25453	-187	315
20060825	23449	20080516	32467	18	630
20060825	23449	20090605	37978	178	1015
20060825	23449	20100521	42988	162	1365
20070112	25453	20080201	30964	-131	385
20070112	25453	20101008	44992	127	1365
20080201	30964	20091127	40483	-118	665
20080201	30964	20100903	44491	-138	945
20091127	40483	20100903	44491	-20	280

Table 3.1: ENVISAT pairs from ascending mode. Interferograms were generated for these SAR pairs. Perpendicular baseline and temporal baseline values are presented for comparison.

Master Date	Master Orbit	Slave Date	Slave Orbit	Perpendicular Baseline (m)	Δt (days)
20051124	19534	20060413	21538	-393	140
20051124	19534	20060622	22540	218	210
20051124	19534	20070712	28051	-196	595
20051124	19534	20070920	29053	301	665

Table 3.2: ENVISAT pairs from descending mode. Interferograms were generated for these SAR pairs. Perpendicular baseline and temporal baseline values are presented for comparison.

illustrated by cycles throughout a predetermined color ramp. Unwrapping of the interferogram refers to the process of converting the interferogram to continuous absolute measurements. Removing the measurement of 2π uncertainty. Unwrapping of the interferogram was performed utilizing the minimum cost flow method (Constantini, 1998). Filtering of interferograms is required to remove phase noise.

The remaining InSAR processing steps required the creation of a displacement map and the backward geocoding of the interferogram to geographic coordinates. The process of creating a displacement map will transform the measurements within the interferogram from units of phase value to meters. Allowing the outputs to be understood by a real world unit of measure. The final step is to create an output that has been backward geocoded from radar coordinates to a geographic coordinate system. The tool will utilize the DEM parameter file again to establish the coordinate system along with additional measurements such as the extents of the data, the pixel size and the pixel spacing throughout the image.

Further analysis and modeling can be performed on the interferograms through the use of a GIS. The interferogram outputs from the backward geocoding step can be brought into a GIS with a few changes made to the image parameters. An output from radar coordinates will be in float format and will consider the origin point the lower left pixel of the image. To properly utilize the images within a GIS, a header (.hdr) file needs to be created for each image. This header file will consist of the number of rows and columns, the x and y coordinate of the origin point and the cellsize. A GIS such as ArcGIS considers the origin point the upper left pixel in the image. Because of this, the upper left corner of the interferogram needs to be calculated from the given location of the lower left pixel transformed to the upper left pixel.

Chapter 4

Results and Discussion

4.1 Results

Concluding InSAR analysis, a continuous presence of deformation was measured. This deformation is apparent as increasing range values or a movement away from the satellite during the elapsed time between data acquisition dates included within the generated interferograms. Movement away from the satellite thus represents an element of subsidence within the study area. The average peak subsidence rates at the Coso site range from as low as approximately 2.5 cm/yr and upwards as much as approximately 3.5 cm/yr. Deformation patterns throughout the Coso site are illustrated in Figures 4.3 to 4.15. Peak subsidence rates at the center of the deformation pattern occur just East-Southeast of Sugarloaf Mountain, the largest rhyolite dome in the volcanic field.

Precise subsidence rates were extracted from each interferogram along transect lines A-A' and B-B' located in Figures 4.1 and 4.2. Figures present the location of transect lines within the local topography as well as within the deformation anomaly. Subsidence rates can be compared comprehensively in Figures 4.16 and 4.17. Graphs showing subsidence rates illustrate the evolution of subsidence increases as the period of time analyzed is increased. These graphs show the distinct bowl of subsidence that is apparent within the Coso geothermal site. Illustrating a sharp downward movement that does not extend laterally out of the geothermal field.

The area of subsidence represents an area approximately 50-55 km^2. This area coincides directly with the boundaries of the presumed location of well sites utilized in geothermal

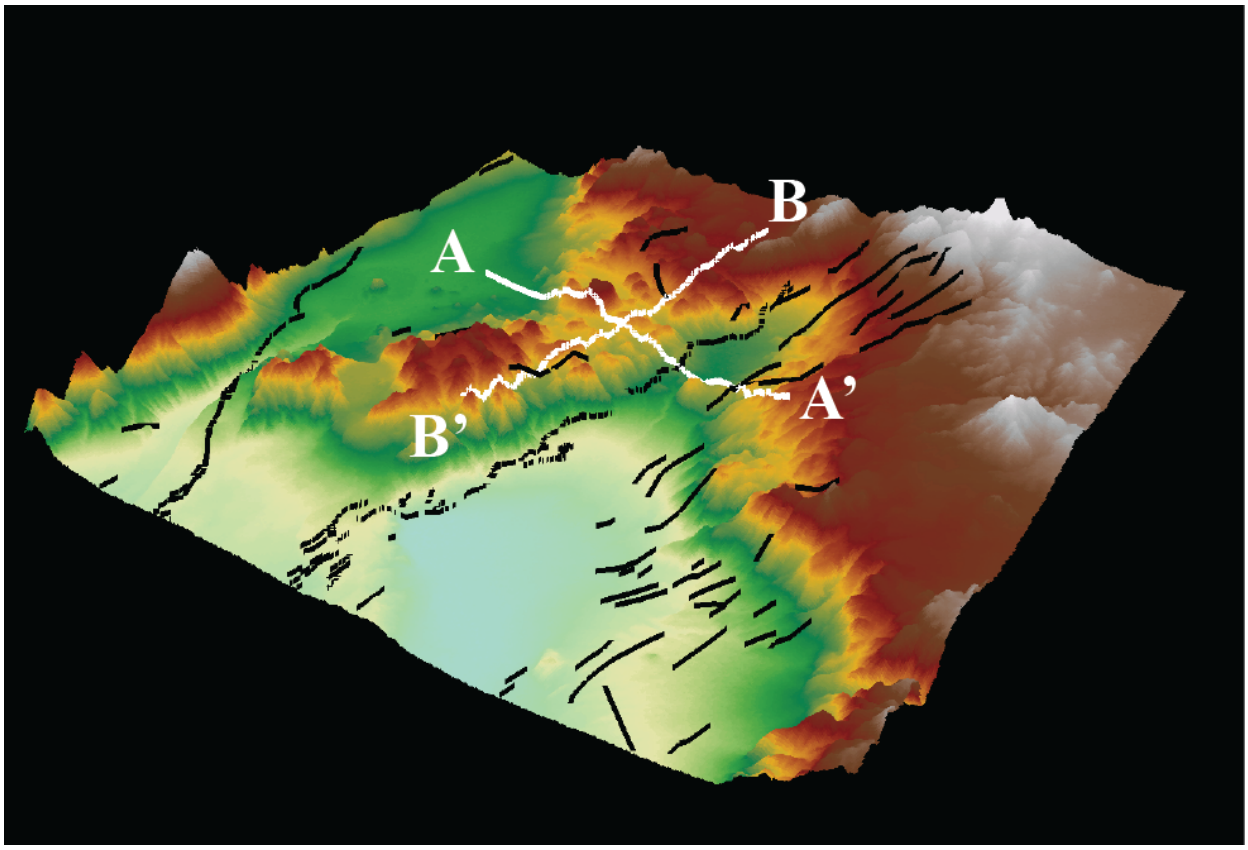

Figure 4.1: 3D topographic map of the Coso Geothermal Site. Black lines represent the active faults active within the Quaternary courtesy of (U.S. Geological Survey, 2006). White lines represent the transect lines that were utilized to extract deformation values displayed in Figures 4.15 and 4.16. Z-value is exaggerated 4 times. Elevation data courtesy of NASA/JPL-Caltech.

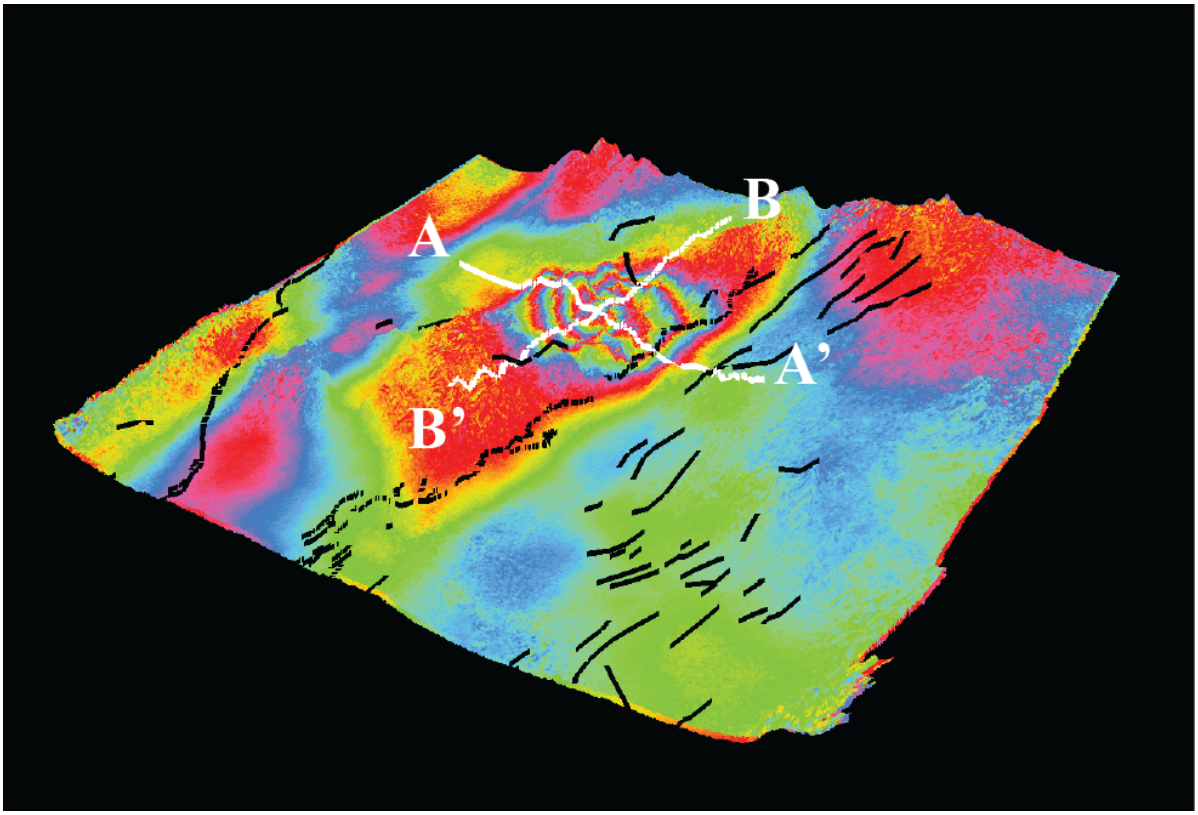

Figure 4.2: 3D Interferogram map of the Coso Geothermal site. Black lines represent the active faults active within the Quaternary courtesy of (U.S. Geological Survey, 2006). Deformation patterns represented by the interferogram represents trends between the years 2006-2010. White lines represent the transect lines that were utilized to extract deformation values displayed in Figures 4.15 and 4.16. Z-value is exaggerated 4 times.

production practices from satellite imagery. The locations of well sites overlain by the extent of the deformation anomaly is illustrated in Figure 4.18. The Coso geothermal site is under operation by private operating companies of the Coso Operating Company and Terra-Gen Power. Information regarding well data and production rates are proprietary and difficult to obtain.

Fialko and Simons (2000) suggested that after 1995 their analysis presented that the subsidence anomaly of the Coso Geothermal site was undergoing an expansion to the South. The interferograms throughout 2005 to 2010 as a part of this research have seen a similar expansion. The subsidence to the South of the main production region is undergoing a more gradual deflation, as the anomaly takes a longer time period of analysis to be of measurable amounts. In addition to this pattern, there appears to be a similar but less developed expansion to the North as time of analysis increases between interferogram pair dates. The expansion along the eastern end of the volcanic field follows a northeast trending direction. Direction of this subsidence expansion parallels the northeast trending faults along the east margin of the volcanic field (Figure 4.2).

Interferograms of the ascending orbit path and the descending orbit path as expected, display slightly different visual details. In the form of subsidence pattern extents to the East and West due to the look direction difference in a side looking fashion. However, subsidence in both the ascending and descending orbit paths are similar in amounts and rates per year.

Earthquake occurrences are included as an overlay upon each interferogram (Figures 4.3-4.15). The displayed earthquakes are representing only earthquakes that have occurred in the Coso site within the time period of the calculated interferogram. Examination for the distribution of earthquake occurrences yields, suggests that there is a significant clustering of seismicity within each center of subsidence. The average rate of seismicity throughout the study period was

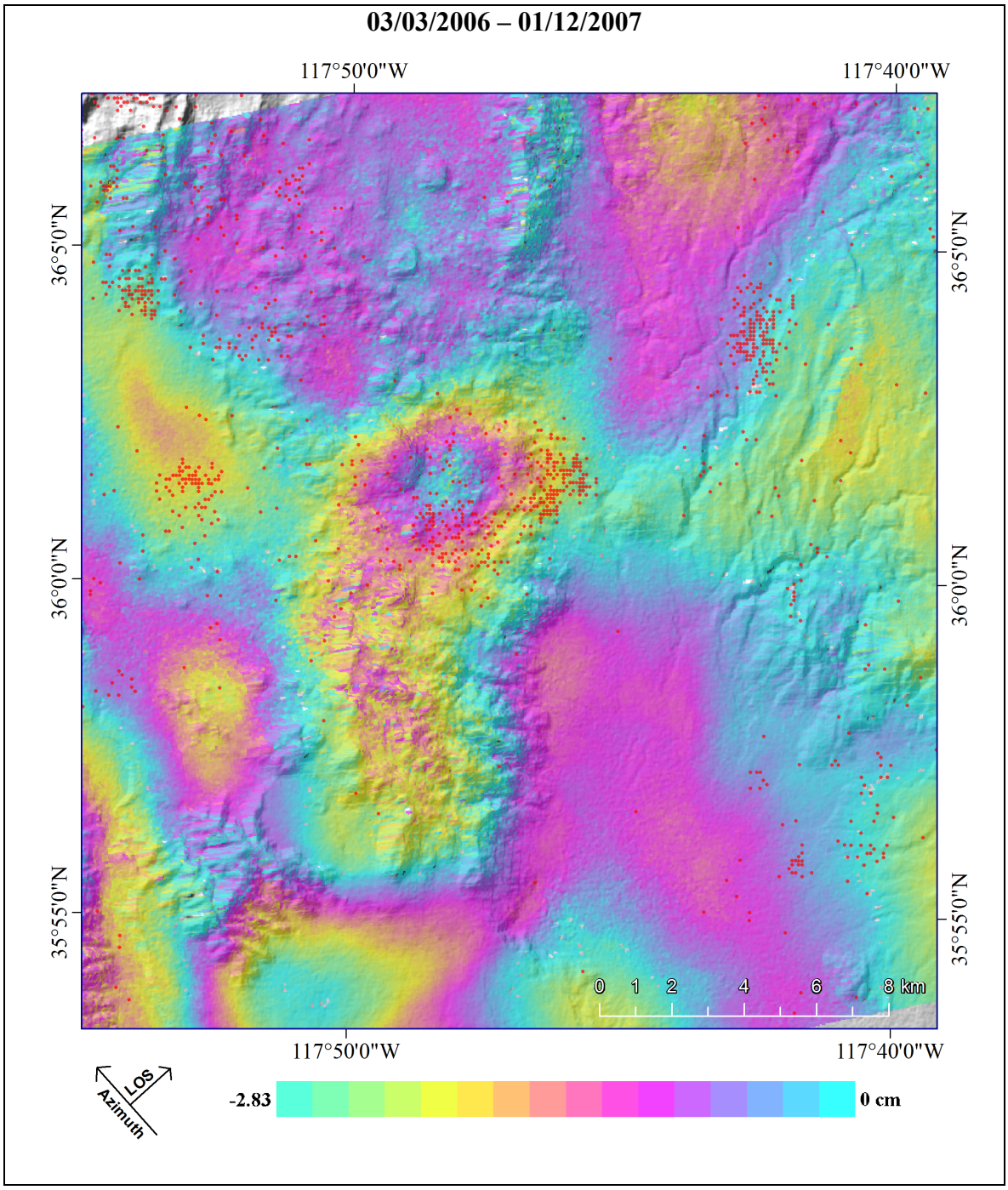

Figure 4.3: Interferogram of the Coso Geothermal site for the period 03/03/2006 to 01/12/2007 overlain on terrain hillshade. Interferogram is generated from ascending mode SAR data from the ENVISAT mission. Interferogram is displayed with a wrapped symbology. Each fringe color cycle represents approximately 2.83 cm of surface change. Total peak subsidence experienced amounts to 2.72 cm. Earthquake occurrences for the time period are represented by red dots courtesy of (SCEDC, 2013). Total occurrences amounts to 1,465 earthquakes.

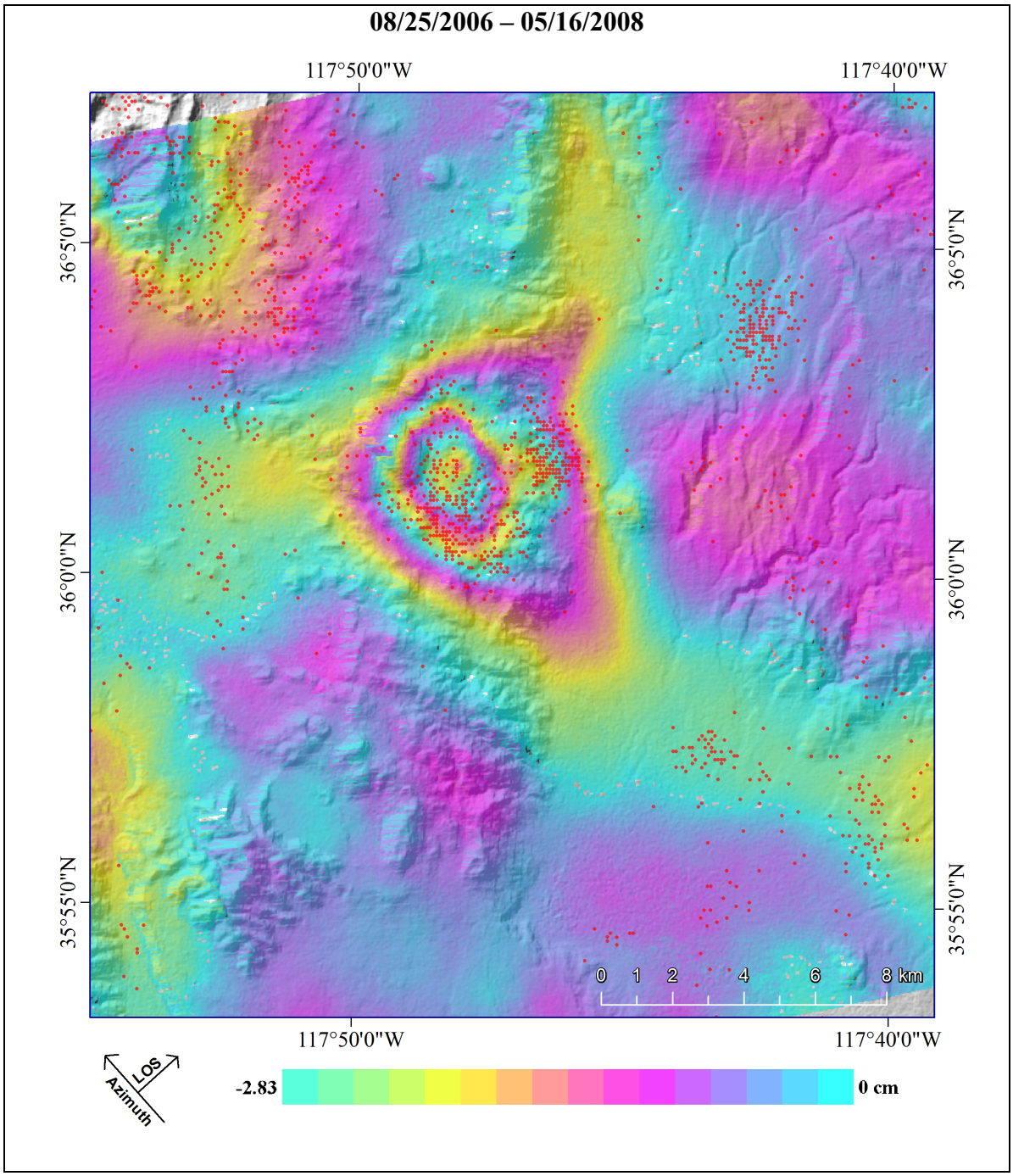

Figure 4.4: Interferogram of the Coso Geothermal site for the period 08/25/2006 to 05/16/2008 overlain on terrain hillshade. Interferogram is generated from ascending mode SAR data from the ENVISAT mission. Interferogram is displayed with a wrapped symbology. Each fringe color cycle represents approximately 2.83 cm of surface change. Total peak subsidence experienced amounts to 4.58 cm. Earthquake occurrences for the time period are represented by red dots courtesy of (SCEDC, 2013). Total occurrences amounts to 1,986 earthquakes.

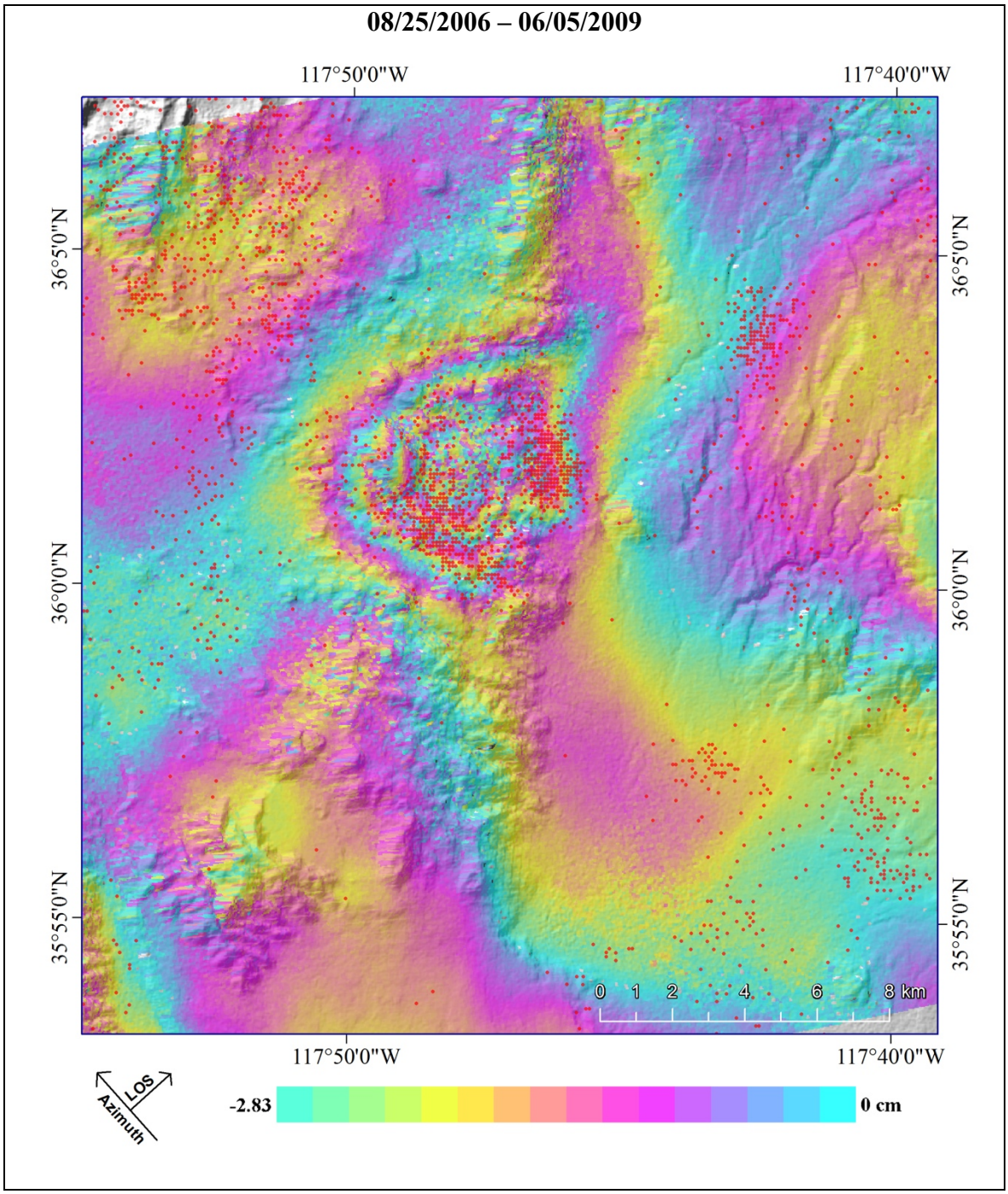

Figure 4.5: Interferogram of the Coso Geothermal site for the period 08/25/2006 to 06/05/2009 overlain on terrain hillshade. Interferogram is generated from ascending mode SAR data from the ENVISAT mission. Interferogram is displayed with a wrapped symbology. Each fringe color cycle represents approximately 2.83 cm of surface change. Total peak subsidence experienced amounts to 7.58 cm. Earthquake occurrences for the time period are represented by red dots courtesy of (SCEDC, 2013). Total occurrences amounts to 3,133 earthquakes.

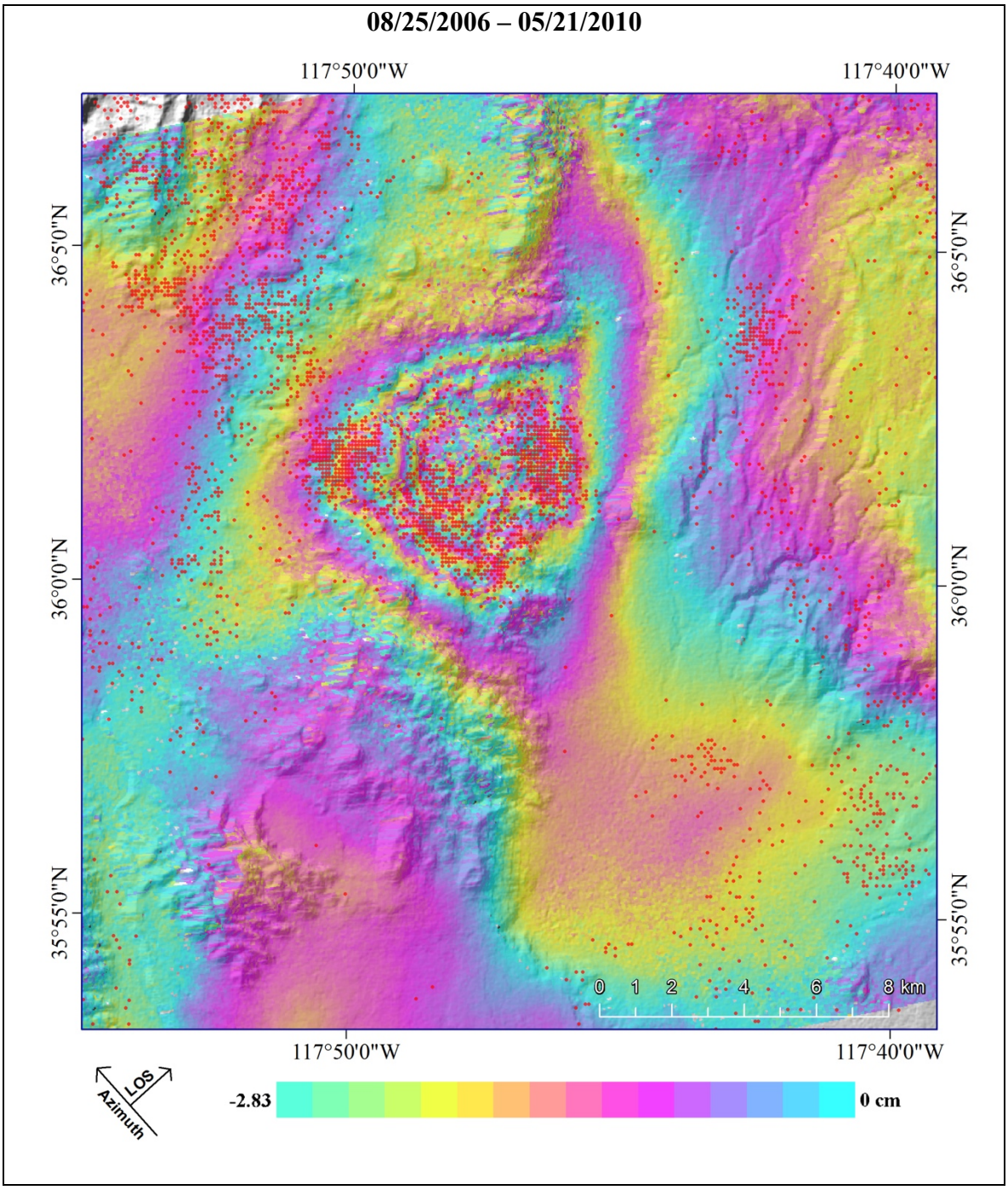

Figure 4.6: Interferogram of the Coso Geothermal site for the period 08/25/2006 to 05/21/2010 overlain on terrain hillshade. Interferogram is generated from ascending mode SAR data from the ENVISAT mission. Interferogram is displayed with a wrapped symbology. Each fringe color cycle represents approximately 2.83 cm of surface change. Total peak subsidence experienced amounts to 8.18 cm. Earthquake occurrences for the time period are represented by red dots courtesy of (SCEDC, 2013). Total occurrences amounts to 4,921 earthquakes.

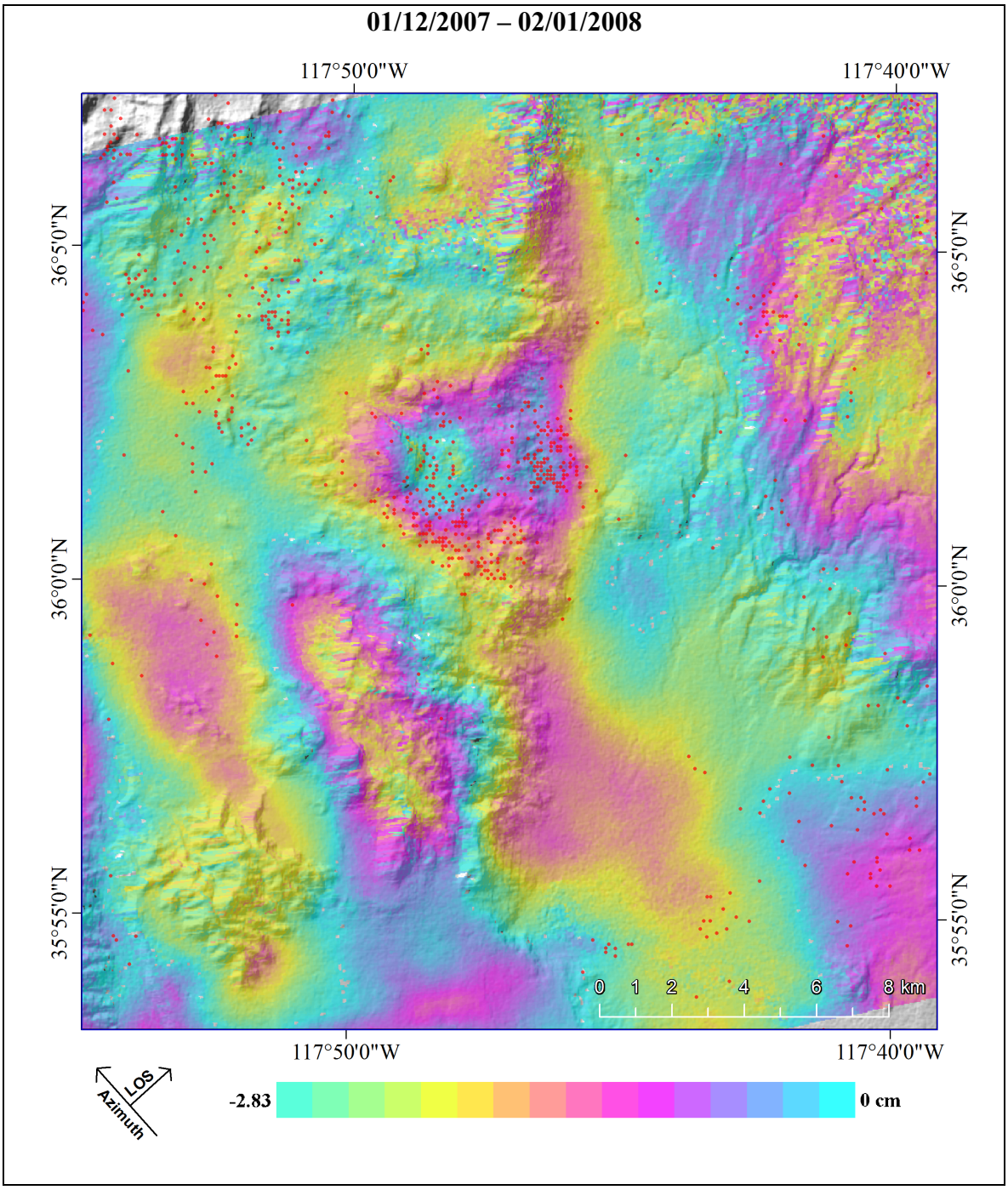

Figure 4.7: Interferogram of the Coso Geothermal site for the period 01/12/2007 to 02/01/2008 overlain on terrain hillshade. Interferogram is generated from ascending mode SAR data from the ENVISAT mission. Interferogram is displayed with a wrapped symbology. Each fringe color cycle represents approximately 2.83 cm of surface change. Total peak subsidence experienced amounts to 3.32 cm. Earthquake occurrences for the time period are represented by red dots courtesy of (SCEDC, 2013). Total occurrences amounts to 1,082 earthquakes.

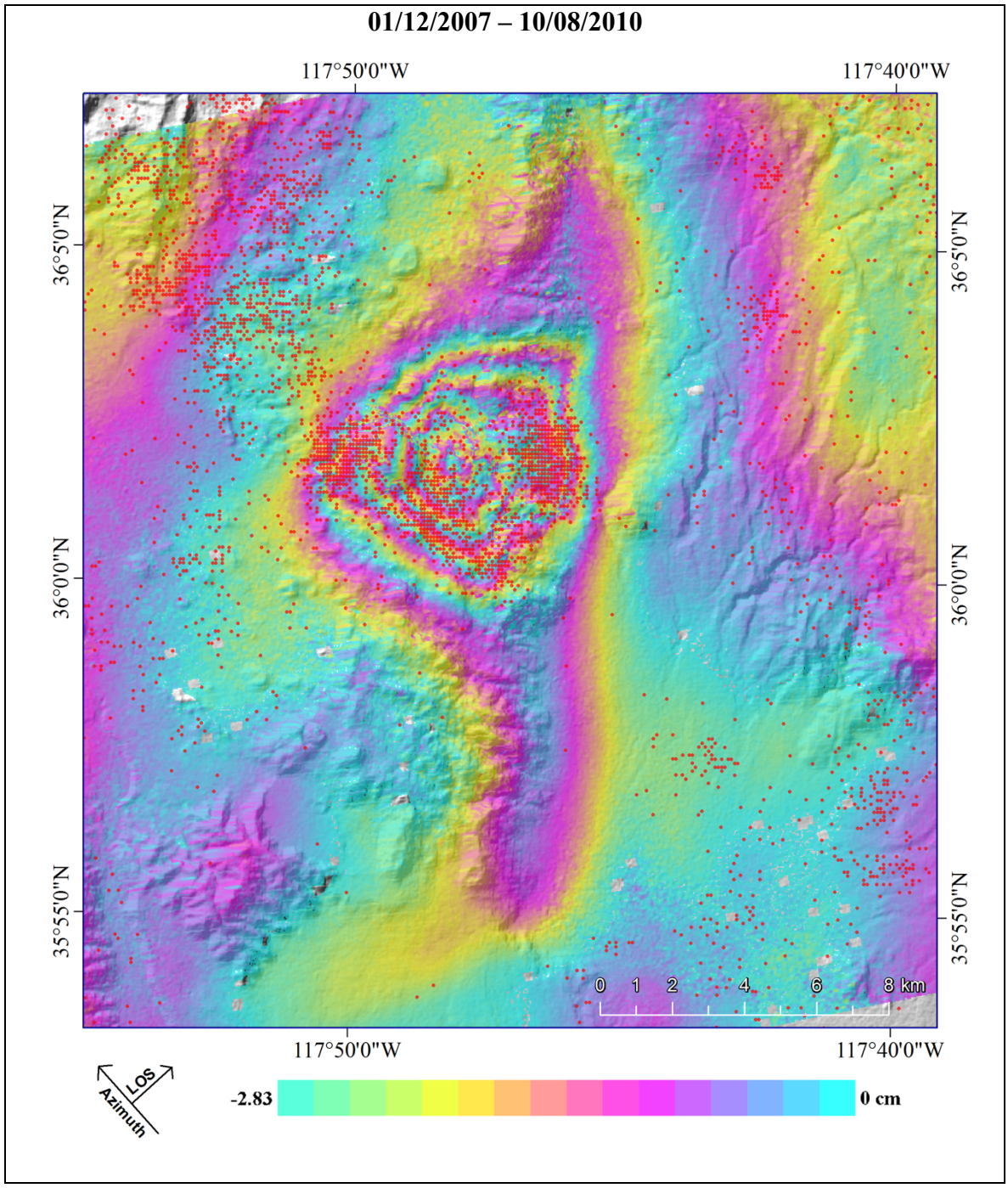

Figure 4.8: Interferogram of the Coso Geothermal site for the period 01/12/2007 to 10/08/2010 overlain on terrain hillshade. Interferogram is generated from ascending mode SAR data from the ENVISAT mission. Interferogram is displayed with a wrapped symbology. Each fringe color cycle represents approximately 2.83 cm of surface change. Total peak subsidence experienced amounts to 10.48 cm. Earthquake occurrences for the time period are represented by red dots courtesy of (SCEDC, 2013). Total occurrences amounts to 4,878 earthquakes.

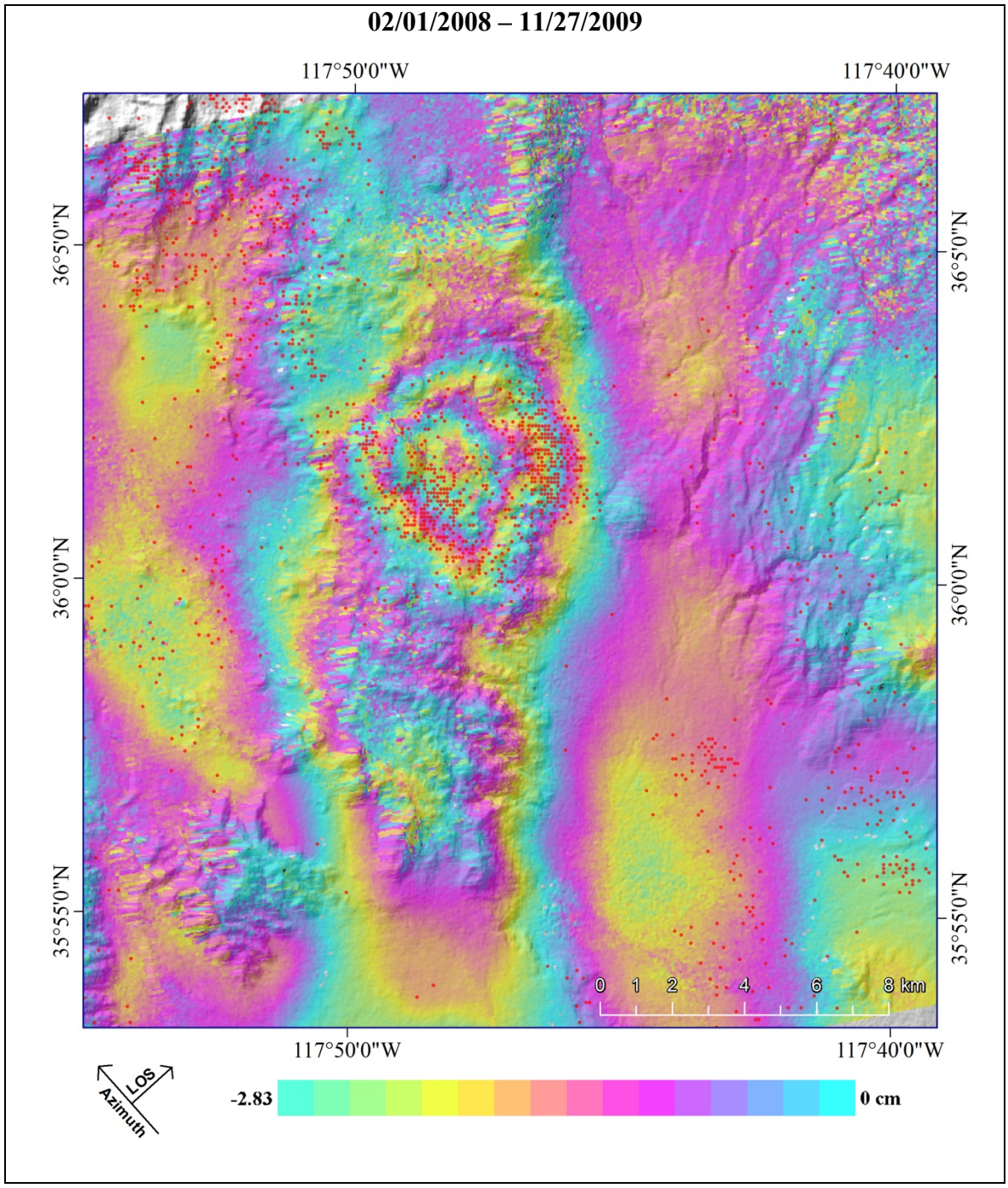

Figure 4.9: Interferogram of the Coso Geothermal site for the period 02/01/2008 to 11/27/2009 overlain on terrain hillshade. Interferogram is generated from ascending mode SAR data from the ENVISAT mission. Interferogram is displayed with a wrapped symbology. Each fringe color cycle represents approximately 2.83 cm of surface change. Total peak subsidence experienced amounts to 5.97 cm. Earthquake occurrences for the time period are represented by red dots courtesy of (SCEDC, 2013). Total occurrences amounts to 1,926 earthquakes.

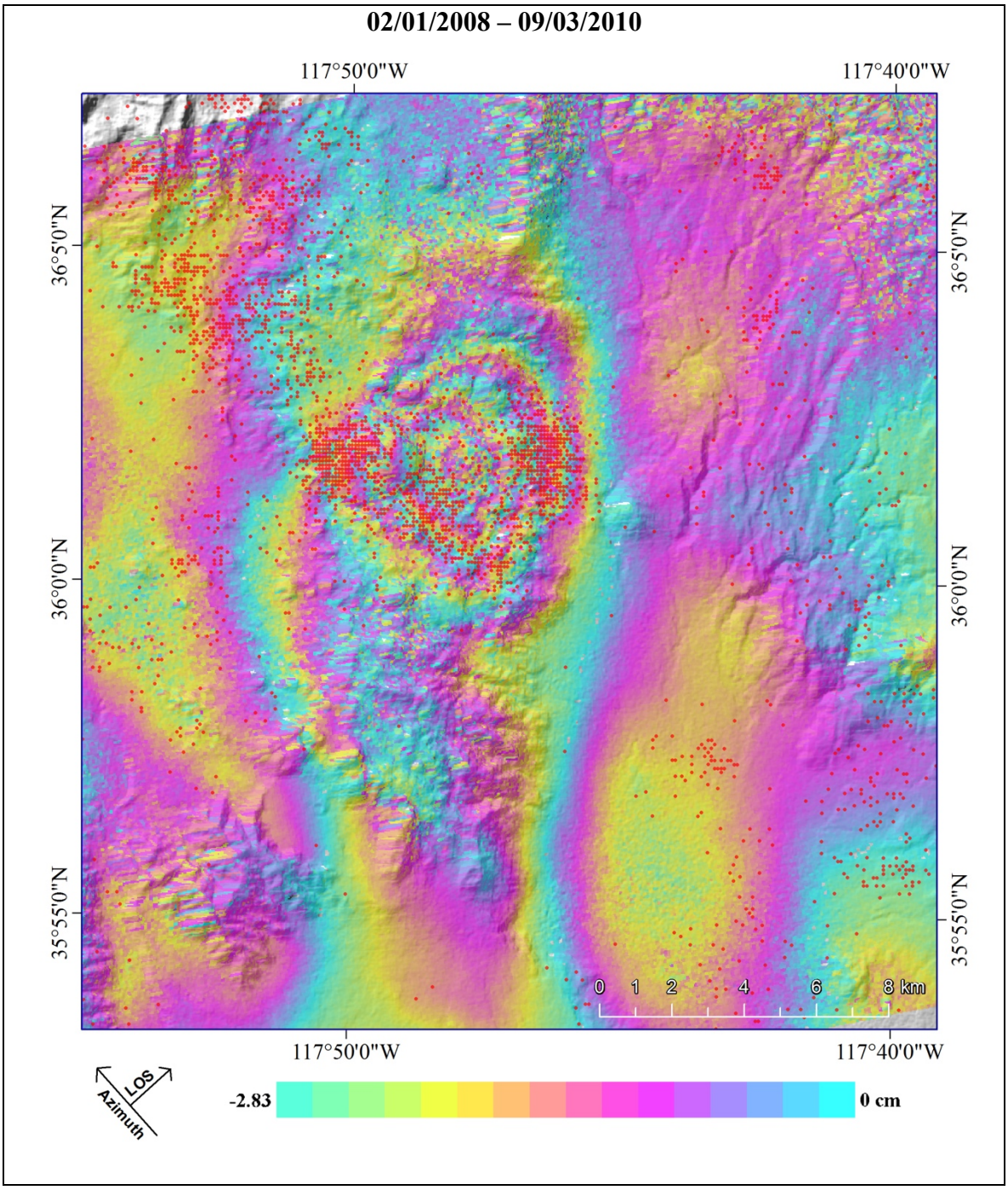

Figure 4.10: Interferogram of the Coso Geothermal site for the period 02/01/2008 to 09/03/2010 overlain on terrain hillshade. Interferogram is generated from ascending mode SAR data from the ENVISAT mission. Interferogram is displayed with a wrapped symbology. Each fringe color cycle represents approximately 2.83 cm of surface change. Total peak subsidence experienced amounts to 8.43 cm. Earthquake occurrences for the time period are represented by red dots courtesy of (SCEDC, 2013). Total occurrences amounts to 3,636 earthquakes.

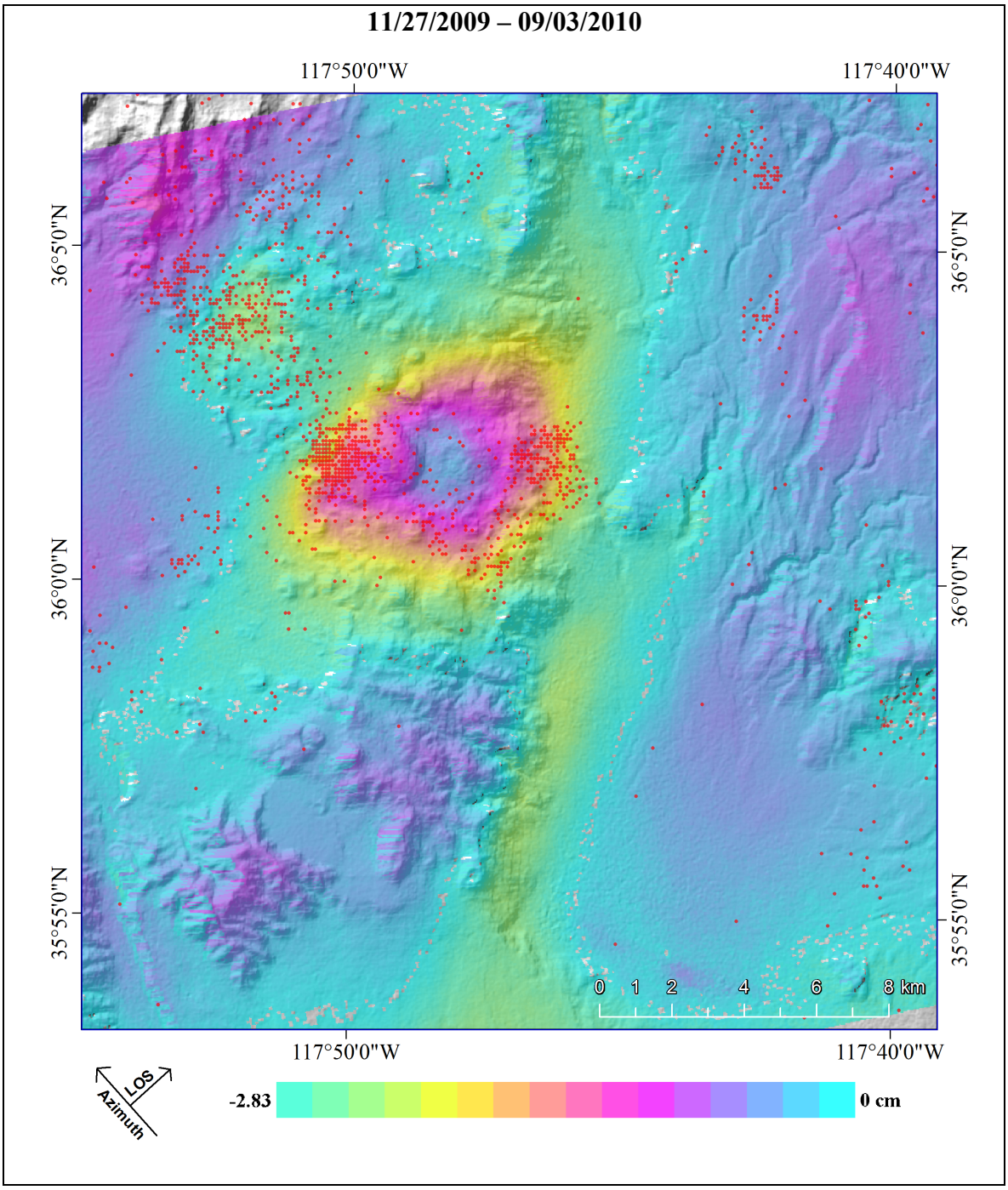

Figure 4.11: Interferogram of the Coso Geothermal site for the period 11/27/2009 to 09/03/2010 overlain on terrain hillshade. Interferogram is generated from ascending mode SAR data from the ENVISAT mission. Interferogram is displayed with a wrapped symbology. Each fringe color cycle represents approximately 2.83 cm of surface change. Total peak subsidence experienced amounts to 1.83 cm. Earthquake occurrences for the time period are represented by red dots courtesy of (SCEDC, 2013). Total occurrences amounts to 1,717 earthquakes.

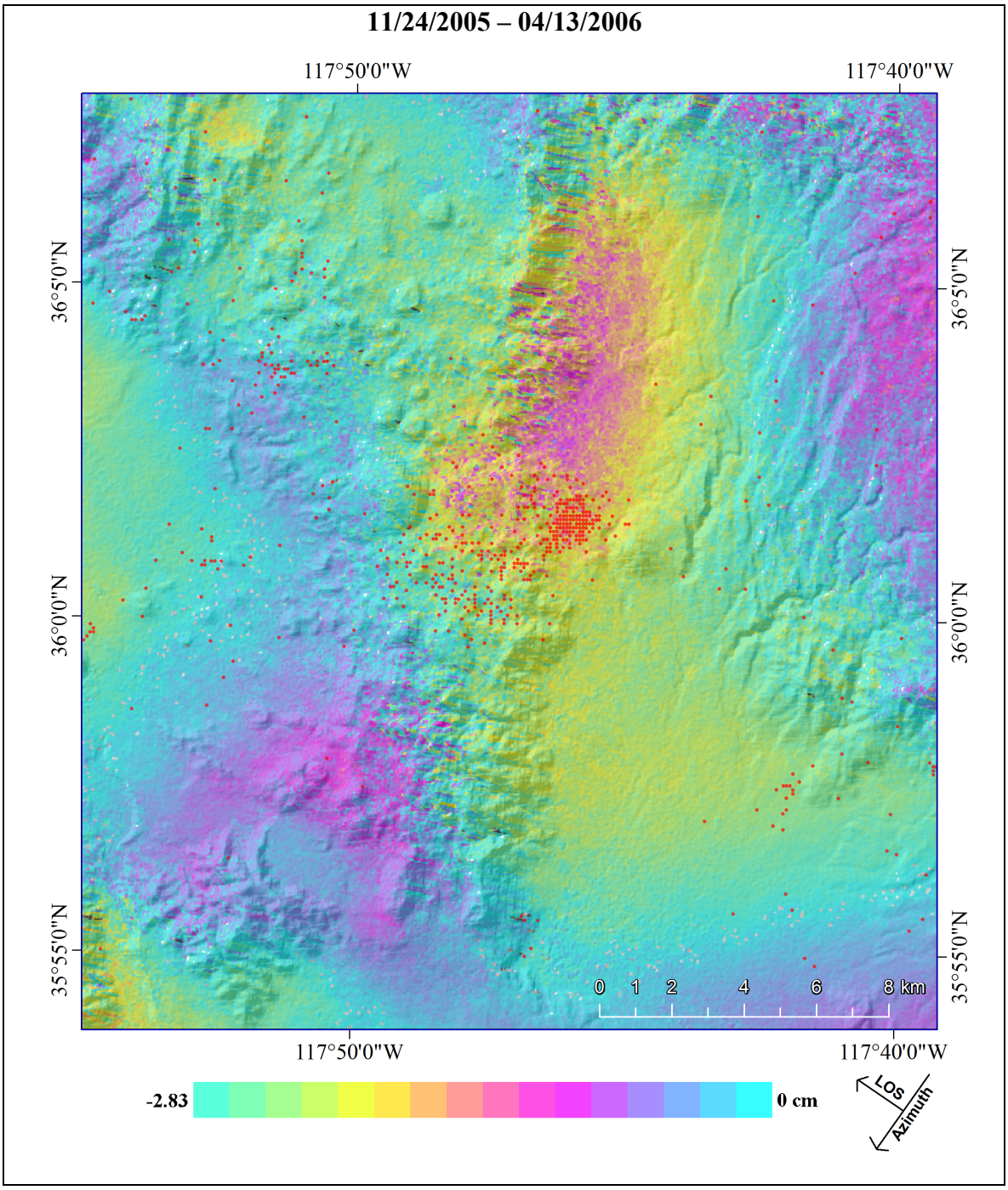

Figure 4.12: Interferogram of the Coso Geothermal site for the period 11/24/2005 to 04/13/2006 overlain on terrain hillshade. Interferogram is generated from descending mode SAR data from the ENVISAT mission. Interferogram is displayed with a wrapped symbology. Each fringe color cycle represents approximately 2.83 cm of surface change. Total peak subsidence experienced amounts to 2.96 cm. Earthquake occurrences for the time period are represented by red dots courtesy of (SCEDC, 2013). Total occurrences amounts to 725 earthquakes.

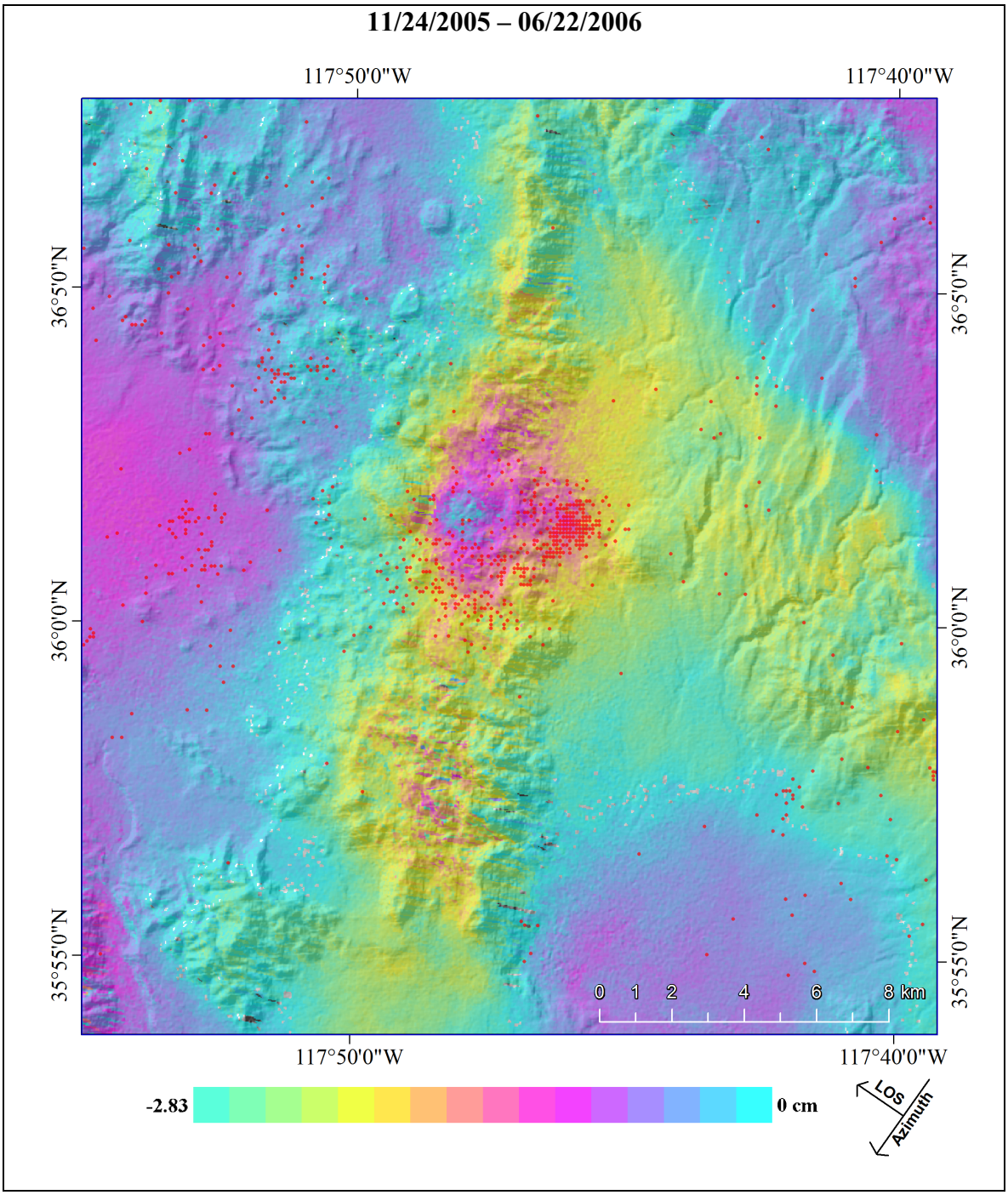

Figure 4.13: Interferogram of the Coso Geothermal site for the period 11/24/2005 to 06/22/2006 overlain on terrain hillshade. Interferogram is generated from descending mode SAR data from the ENVISAT mission. Interferogram is displayed with a wrapped symbology. Each fringe color cycle represents approximately 2.83 cm of surface change. Total peak subsidence experienced amounts to 2.37 cm. Earthquake occurrences for the time period are represented by red dots courtesy of (SCEDC, 2013). Total occurrences amounts to 925 earthquakes.

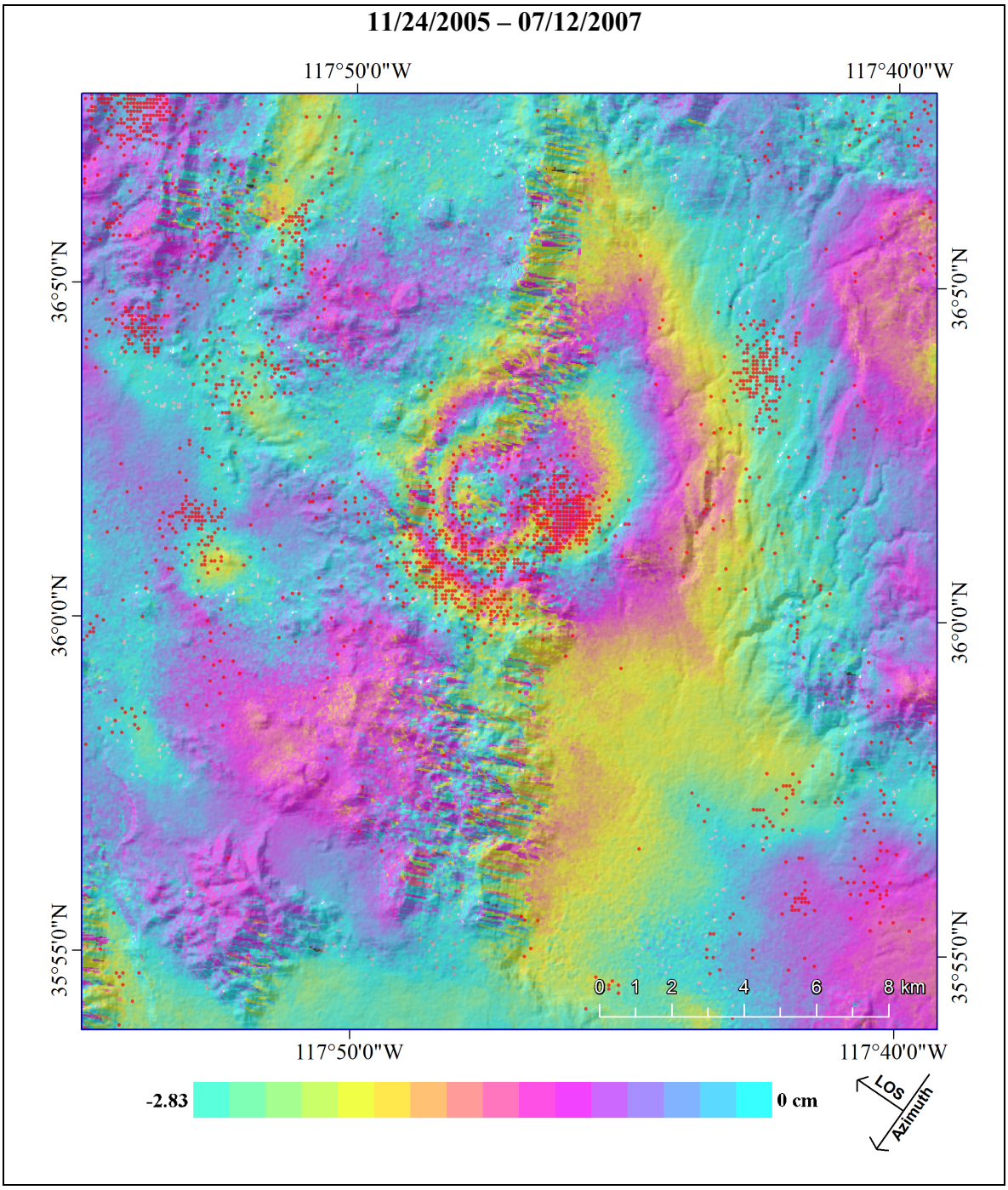

Figure 4.14: Interferogram of the Coso Geothermal site for the period 11/24/2005 to 07/12/2007 overlain on terrain hillshade. Interferogram is generated from descending mode SAR data from the ENVISAT mission. Interferogram is displayed with a wrapped symbology. Each fringe color cycle represents approximately 2.83 cm of surface change. Total peak subsidence experienced amounts to 5.49 cm. Earthquake occurrences for the time period are represented by red dots courtesy of (SCEDC, 2013). Total occurrences amounts to 2,506 earthquakes.

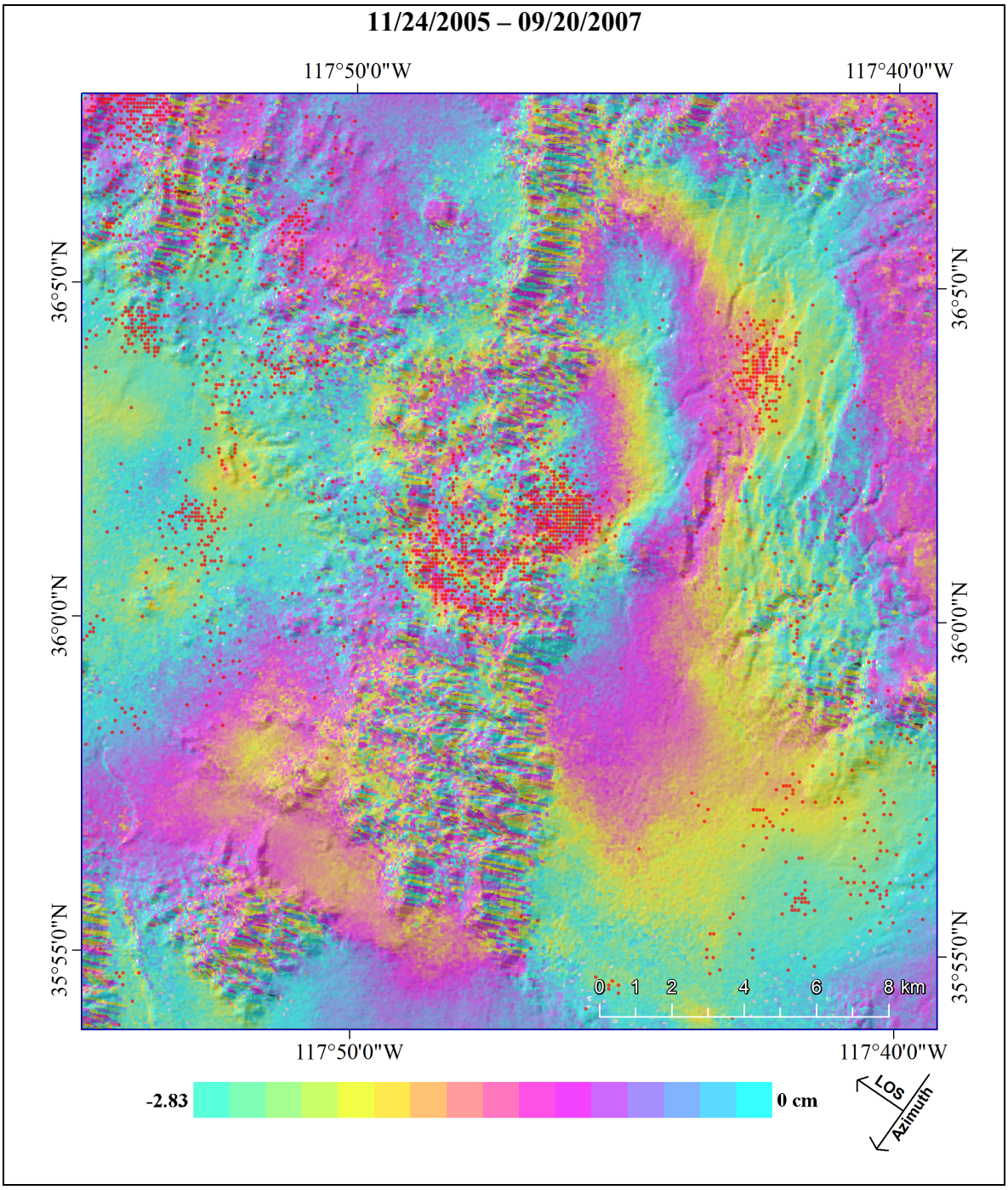

Figure 4.15: Interferogram of the Coso Geothermal site for the period 11/24/2005 to 09/20/2007 overlain on terrain hillshade. Interferogram is generated from descending mode SAR data from the ENVISAT mission. Interferogram is displayed with a wrapped symbology. Each fringe color cycle represents approximately 2.83 cm of surface change. Total peak subsidence experienced amounts to 6.39 cm. Earthquake occurrences for the time period are represented by red dots courtesy of (SCEDC, 2013). Total occurrences amounts to 2,753 earthquakes.

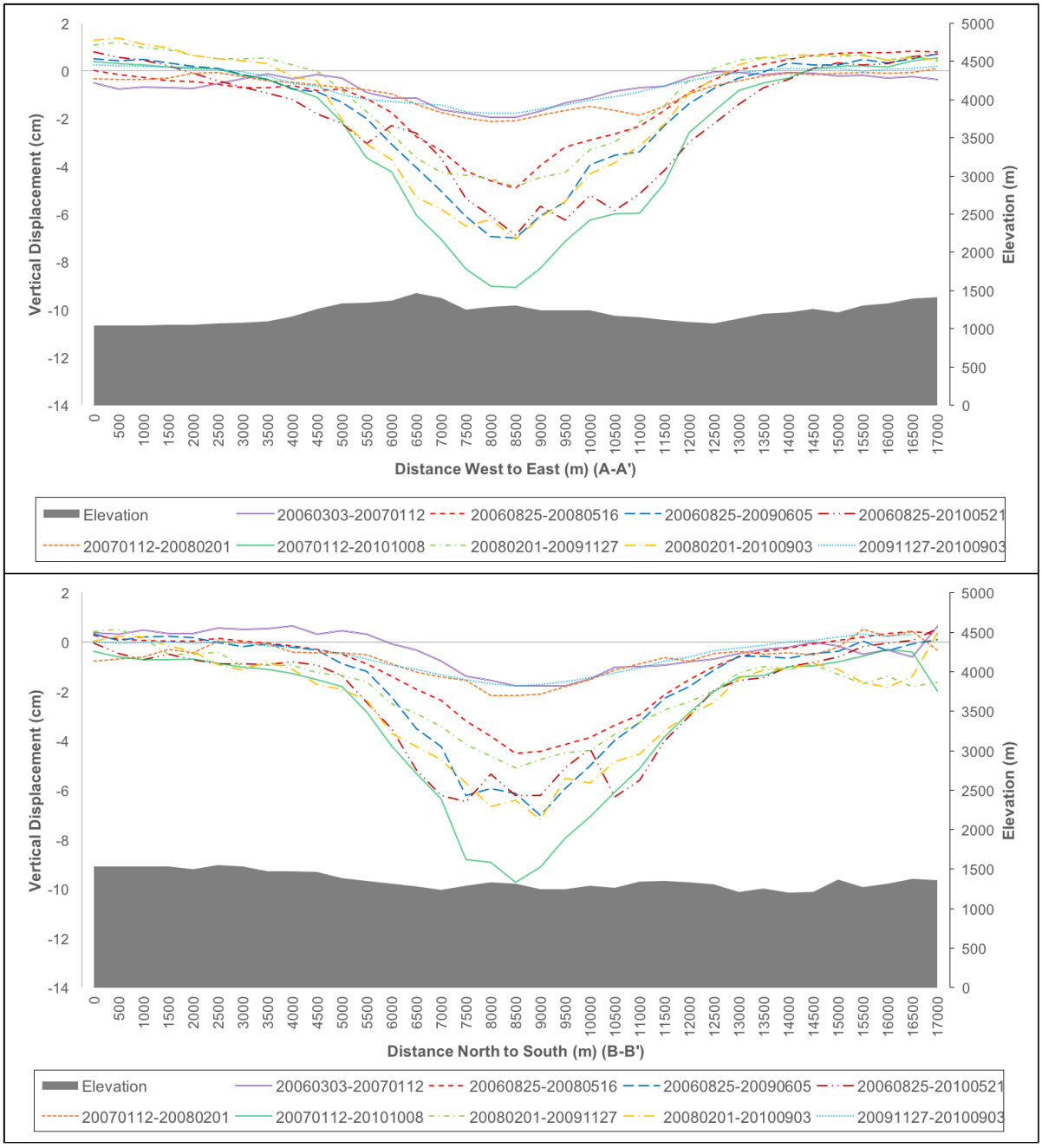

Figure 4.16: Ascending mode SAR data deformation values plot. Transects A-A' and B-B' locations are displayed in Figure 4.1. Deformation values from each interferogram were taken along transect lines.

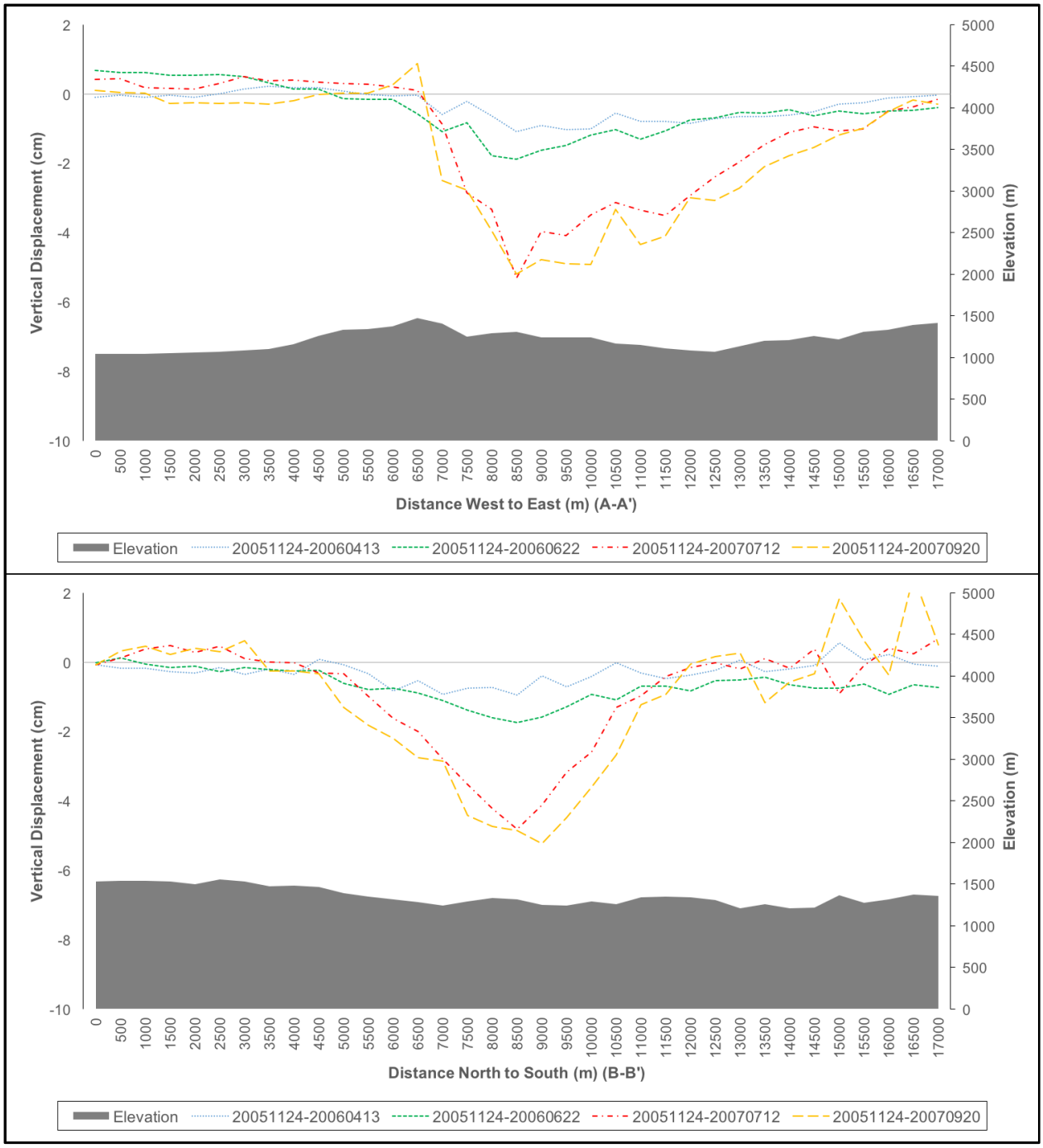

Figure 4.17: Descending mode SAR data deformation values plot. Transects A-A' and B-B' locations are displayed in Figure 4.1. Deformation values from each interferogram were taken along transect lines.

approximately 1,200 per year. The rate of earthquake occurrences ranges between 700 to 1500 annually. Difficulties are found in a tectonic setting such as the Coso site in determining a clear designation on what is directly connected to geothermal production practices and what is a result of natural tectonic movements throughout the region.

4.2 Discussion

In a region such as the Coso site, many factors can provide a leading cause to subsidence as exhibited there. Many natural forces may play a role in the deflation of the geothermal zone due to the high tectonic activity and the development of the volcanic system over time. Analysis of subsidence patterns provide support as the overwhelming impact of geothermal production practices form a likely cause to the localized and distinct subsidence exhibited within the site throughout the previous two decades.

Rates of subsidence amounting to approximately 2.5 to 3.5 cm/year, display a change in the Earth's surface that moves with relative similarity per year. Separated by less than a centimeter difference between individual interferograms in annual rates of subsidence. This correlation suggests a steady state of deformation is taking place in the Coso Geothermal site. This rate of subsidence continues the trends presented by Fialko and Simons (2000) and Wicks et al (2001) throughout the 1990s. They concluded that subsidence rates amounted to approximately 3.5 cm/year. They concluded from inverse modeling methods that a short wavelength (2 km) deformation was taking place within the Coso Geothermal site that is characteristic from a source of geothermal production impacts. The timeline methods of analysis presented within this research characterizes this same form of deformation within the localized study area surrounding the active geothermal production field. Similar methods have been

emplaced to analyze deformation in active geothermal fields that concluded subsidence as a result of pumping mechanisms associated with geothermal production practices (Carnec and Fabriol, 1999; Sarychikhina et al, 2010; Ali et al, 2015).

The presence of active geothermal production practices in the Coso site for the previous <30 years raises concern to the impact that production methods can have on the subsidence anomaly experienced. Illustrated in Figure 4.18, the distribution of presumed geothermal production wells throughout the Coso site are shown as the stations of man-made buildings scattered across the surface. An overlay of the deformation anomaly area is displayed with an interferogram covering a 2007 to 2010-time period. From this comparison it can be seen that the focal area of the Coso site that is undergoing subsidence is directly correlated with the presumed extents of geothermal production areas currently under operation.

Factors of geothermal operations can be attributed to this pattern of subsidence surrounding the production area. The Coso Operating Company (2008) set forth a proposal amid controversy, that would allow the company to pump water from the nearby Rose Valley basin. The pumping would consist of a rate of 4,800 acre-feet per year. The proposal was approved and pumping of water from Rose Valley began in 2009 where it will be used for injection as well as cooling of geothermal facilities. A move by the operating company to impede on the immense deficit of fluids and pressure within the Coso geothermal reservoir. Factors inspiring this mode of operation come from the reports of the Coso Operating Company (2008) that states production methods yield only a 50% percent return of fluids that are extracted. These fluids are extracted, flashed to steam for energy production and then reinjected. An extended period of such operations have contributed to a depressurization of the reservoir over the greater than 20 years of production. Adams (2000) have suggested the development of a vapor-dominated zone within

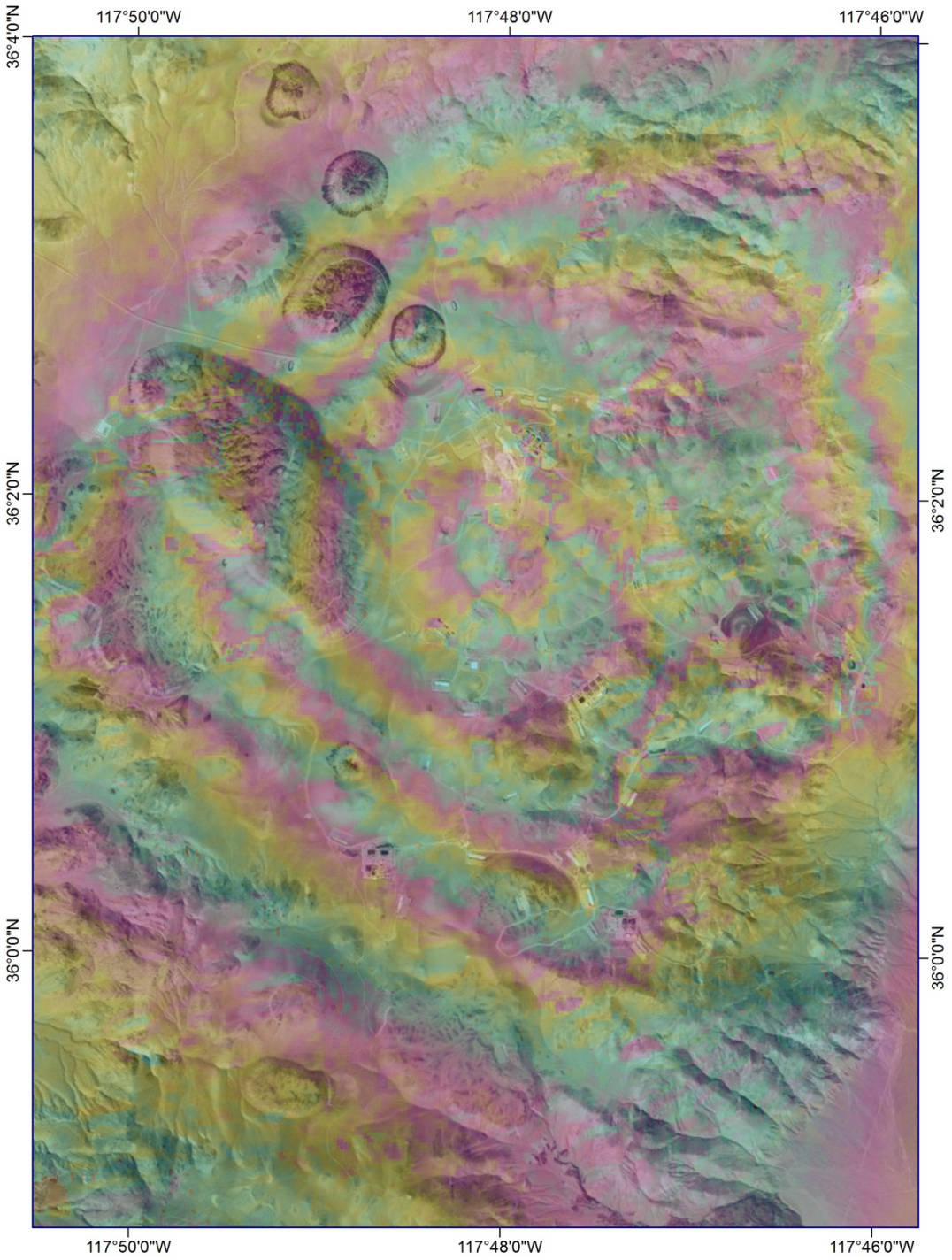

Figure 4.18: Location of Coso Geothermal production wells. Area of subsidence derived from interferogram calculation between the years 2007 and 2010 overlain by satellite imagery portraying presumed location of production wells courtesy of (ESRI, 2016).

the reservoir as a result of the depressurization.

While rates of subsidence are relatively steady within a centimeter of change in rates, there is some fluctuation. Depending on the year intervals that were selected for analysis in individuals interferograms. Rates of subsidence varied between ~2.5 to ~3.5 cm/yr. While some variance could be attributed to atmospheric effects in the imaging process, the variability could suggest a not completely constant impact of subsidence. This could likely be a result of fluctuating production methods. That will vary depending on production needs for each borehole location. Contrasting a natural source of deformation such as a leaking magmatic system deriving from tectonic influences of extensional strain as suggested by Bacon et al (1980) that likely provides a more consistent annual rate of subsidence.

Local seismicity can highlight the impact of activity levels that practices such as geothermal production are putting on the system. In a highly tectonic region such as the Coso site, levels of seismicity, mostly consisting of micro-seismicity will be present at any time. These levels of seismicity can be referred to as background seismicity. It is difficult to differentiate the background seismicity from that which is a direct response to the production practices from injection of fluids into the ground. Significant clustering of seismicity can be used as evidence to support the claim whether there is any sense of correlation between local production impacts on the region at a level exceeding the natural background seismicity.

Earthquake records are included in the interferograms within Figures 4.3c to 4.15c. Earthquake records are included as an overlay to the interferogram of the designated time period. Only earthquake records coinciding with that time period are displayed. The overlay allows the analysis of such in determining the degree at which clustering of seismicity is occurring. Conclusions that can be established from this examination show that there is significant

clustering within the subsidence anomaly present at the Coso site. Knowledge gained from this concludes that there is a significant degree of impact that is present on the system by production methods. The highly clustered earthquake occurrences consist of primarily micro-seismicity with few outliers of small earthquakes (<3 magnitude). Feng and Lees (1998) supported the distinction of subsidence occurrences occurring as a result of geothermal production practices with the association of high seismicity levels in regard to borehole locations within the geothermal field.

Chapter 5

Future Directions

Many steps can be taken to improve or expand upon results that are presented as a part of this research. Some methods may consist of implementing more SAR data from additional satellite missions. To expand upon the period of study additional GIS or auxiliary data may be included to refine the results. This may lead to a more precise conclusion on the true deformation impact that is taking place in this highly active zone of tectonism. Understanding the subsurface changes may provide an additional method to building a concise analysis of this region as a whole.

SAR data from additional satellite missions such as ERS-2 as well as Sentinel-1 will expand that years of analysis that are a part of this research. ERS-2 data can expand the years of analysis to earlier time periods than analyzed here. Including additional years between 2000 to 2005 will account for an extension into the years that were not included in previous studies from the 1990s. As well as include an additional five years to the data presented here. Including Sentinel-1 data will likewise expand the study period. Sentinel-1 data will provide an even more modern set of data from 2014 to the present. This will provide the newest deformation trends that have occurred in recent years. Inclusion of these additional data sets would create a more comprehensive and robust analysis while providing the potential to exposing any trends that may have been overlooked by the results presented as a part of this research. Including data up to the present would also provide an analysis of the Coso site in a time period after the Coso Operating Company began pumping water from the nearby Rose Valley reservoir for injection. This analysis would highlight whether or not these additional measures have made a positive impact

on the deflation of the geothermal system or not.

A potentially valuable form of additional data to add to this research is the location of drilling holes throughout the geothermal production fields in the Coso region. The well data would allow knowledge of where the exact location that geothermal production practices are occurring. Along with the designations of each well to their usage. May they be an injection, extraction or injection/extraction wells. Having this knowledge may provide the necessary information to be able to decipher whether local peaks of deformation during the study periods can be correlated to one of the well locations.

The final beneficial addition to this research consists of the incorporation of inverse modeling to understand the evolution of the subsurface over the same study period. The results generated from the interferogram calculations can be utilized to perform inverse modeling of the subsurface of the Coso geothermal site. Multiple variations of point source models can be applied (Mogi, 1958; Okada, 1985; Yang, 1988). The complexity of the deformation exhibited at the Coso geothermal site will determine the applicability of an individual point source model over the others. Performing this analysis will provide the ability to infer the depth and dimensions of a potential source for the geothermal system at depth. Knowing this enables the possibility to model this source over the established study period to provide a conclusion on the evolution of the source over time as it has impacted surface changes. This form of information may provide a clearer understanding as to why the surface deformation is occurring.

Chapter 6

Conclusions

Necessary methods and data required for an analysis of deformation trends throughout a designated region is presented in this research. A cutting edge remote sensing technique known as Interferometric Synthetic Aperture Radar (InSAR) is utilized for the performance of surface movement analysis. This technique provides the necessary precision to measure differentiating slow and rapid shifts in the surface location over time. Two-pass differential interferometry methods were employed for the generation of interferograms, of which visually and quantitatively present the deformation trends throughout a designated study period in the form of an image that contains phase values within pixels, to form an overall grid of the region.

InSAR analysis was performed throughout the Coso Geothermal site in eastern California. The analysis covered the years between 2005 to 2010. Local subsidence was measured in the Coso site amounting to a range of 2.5 to 3.5 cm/year throughout an area of approximately 50 to 55 km^2. The local subsidence anomaly is concluded to be a direct surface response to the geothermal production procedures that are employed within the site. Extraction and reinjection of fluids as a practice of production methods has created a net loss of fluid within the geothermal system resulting in depressurization throughout the system. Depressurization provides the mechanisms for the experienced subsidence creating a cone of deflation at the Coso site. Additionally, support of the subsidence relation to production methods are displayed as the extents of the subsidence anomaly coincide directly with the visible locations of production wells at the Coso site.

This research employs InSAR techniques to infer the on-going deformation patterns and

magnitudes present at the Coso site. Previous work sought to analyze this anomaly throughout the 1990s. While this work extends this knowledge base throughout 2005-2010. The steady rate of deformation measured in this analysis as well as the correlation of similar deformation rates of the 1990s suggests that the deformation experienced within the Coso site is a result of linear deformation. Likely brought on as a continuation of depressurization due in part to the continual extraction of hydrothermal fluids.

References

Adams, Michael C., et al. "Geologic history of the Coso geothermal system." *Transactions-Geothermal Resources Council* (2000): 205-210.

Ali, S. T., et al. "InSAR measurements and numerical models of deformation at Brady Hot Springs geothermal field (Nevada), 1995-2012." *AGU Fall Meeting Abstracts*. Vol. 1. 2013.

Aly, Mohamed H., and Elizabeth S. Cochran. "Spatio-temporal evolution of Yellowstone deformation between 1992 and 2009 from InSAR and GPS observations." *Bulletin of volcanology* 73.9 (2011): 1407-1419.

Aly, M. H., D. W. Rodgers, and G. D. Thackray. "Differential Synthetic Aperture Radar Interferometry to Investigate Surface Deformation of the Eastern Snake River Plain, Idaho, USA." *The Journal of Geology* 117.1 (2009): 103-108.

Aly, M. H., et al. "Permanent Scatterer investigation of land subsidence in Greater Cairo, Egypt." *Geophysical Journal International* 178.3 (2009): 1238-1245.

Bacon, Charles R., Wendell A. Duffield, and Kazuaki Nakamura. "Distribution of Quaternary rhyolite domes of the Coso Range, California: Implications for extent of the geothermal anomaly." *Journal of Geophysical Research: Solid Earth* 85.B5 (1980): 2425-2433.

Bamler, Richard, and Philipp Hartl. "Synthetic aperture radar interferometry." *Inverse problems* 14.4 (1998): R1.

Berardino, Paolo, et al. "A new algorithm for surface deformation monitoring based on small baseline differential SAR interferograms." *Geoscience and Remote Sensing, IEEE Transactions on* 40.11 (2002): 2375-2383.

Bhattacharyya, Joydeep, and Jonathan M. Lees. "Seismicity and seismic stress in the Coso Range, Coso geothermal field, and Indian Wells Valley region, southeast-central California." *Mem. Geol. Soc. Am* 195 (2002): 243-257.

Bürgmann, Roland, Paul A. Rosen, and Eric J. Fielding. "Synthetic aperture radar interferometry to measure Earth's surface topography and its deformation." *Annual Review of Earth and Planetary Sciences* 28.1 (2000): 169-209.

“California climate zone 14.” Pacific Gas and Electric Company. <http://www.pge.com/includes/docs/pdfs/about/edusafety/training/pec/toolbox/arch/climate/california_climate_zone_14.pdf>.

Carnec, Claudie, and Hubert Fabriol. "Monitoring and modeling land subsidence at the Cerro Prieto geothermal field, Baja California, Mexico, using SAR interferometry." *Geophysical Research Letters* 26.9 (1999): 1211-1214.

Combs, Jim. "Heat flow in the Coso geothermal area, Inyo County, California." *Journal of Geophysical Research: Solid Earth* 85.B5 (1980): 2411-2424.

“Copernicus: Sentinel-1 – The SAR imaging constellation for land and ocean services.” EOPortal Directory: European Space Agency. <https://directory.eoportal.org/web/eoportal/satellite-missions/c-missions/copernicus-sentinel-1>.

Costantini, Mario. "A novel phase unwrapping method based on network programming." *Geoscience and Remote Sensing, IEEE Transactions on* 36.3 (1998): 813-821.

Coso Operating Company, Hay Ranch Water Extraction and Delivery System. “Hydrology and water quality.” Appendix H, Section 3.2, Conditional Use Permit (CUP 2007-003) Application, 2008, Draft EIR.

“Coso Valley groundwater basin.” South Lahontan hydrologic region; California’s Groundwater Bulletin 118.

Curlander, John C., and Robert N. McDonough. *Synthetic aperture radar*. New York, NY, USA: John Wiley & Sons, 1991.

Danskin, Wesley R. *Evaluation of the hydrologic system and selected water-management alternatives in the Owens Valley, California*. Vol. 2370. US Department of the Interior, US Geological Survey, 1999.

Davatzes, Nicholas C., and S. Hickman. "Controls on fault-hosted fluid flow: Preliminary results from the Coso Geothermal Field, CA." *Geothermal Resources Council Transactions* 29 (2005): 343-348.

Dokka, Roy K., and Christopher J. Travis. "Role of the eastern California shear zone in accommodating Pacific-North American plate motion." *Geophysical Research Letters* 17.9 (1990): 1323-1326.

Dongchen, E., Chunxia Zhou, and Mingsheng Liao. "Application of SAR interferometry on DEM generation of the Grove Mountains." *Photogrammetric Engineering & Remote Sensing* 70.10 (2004): 1145-1149.

Duell Jr, L. F. "Estimates of evapotranspiration in alkaline scrub and meadow communities of Owens Valley, California, using the Bowen-ratio, eddy-correlation, and Penman-combination methods." *Water Supply Papers-US Geological Survey* 2370-E (1990).

Duffield, Wendell A., Charles R. Bacon, and G. Brent Dalrymple. "Late Cenozoic volcanism, geochronology, and structure of the Coso range, Inyo County, California." *Journal of Geophysical Research: Solid Earth* 85.B5 (1980): 2381-2404.

“EnviSat (Environmental satellite).” EOPortal Directory: European Space Agency. <https://directory.eoportal.org/web/eoportal/satellite-missions/e/envisat>.

“ERS-1 (European remote-sensing satellite-1).” EOPortal Directory: European Space Agency. <https://directory.eoportal.org/web/eoportal/satellite-missions/e/ers-1>.

“ERS-2 (European remote-sensing satellite-2).” EOPortal Directory: European Space Agency. <https://directory.eoportal.org/web/eoportal/satellite-missions/e/ers-2>.

ESRI. ArcGIS Desktop 10: Release 10.3. Redlands, CA: Environmental Systems Research Institute. (2016). World Imagery Sources: Esri, DigitalGlobe, geoeye, i-cubed, USDA FSA, USGS, AEX, Getmapping, Aerogrid, IGN, IGP, swisstopo, and the GIS User Community.

Farr, Tom G., and Mike Kobrick. "Shuttle Radar Topography Mission produces a wealth of data." *Eos, Transactions American Geophysical Union* 81.48 (2000): 583-585.

Feng, Qiuchun, and Jonathan M. Lees. "Microseismicity, stress, and fracture in the Coso geothermal field, California." *Tectonophysics* 289.1 (1998): 221-238.

Feretti, A., Monti-Guarnieri, A., Prati, C., and Rocca, F., “InSAR principles: Guidelines for SAR interferometry processing and interpretation.” ESA Publications; Vol. 19, 2007.

Ferretti, Alessandro, Claudio Prati, and Fabio Rocca. "Nonlinear subsidence rate estimation using permanent scatterers in differential SAR interferometry." *Geoscience and Remote Sensing, IEEE transactions on* 38.5 (2000): 2202-2212.

Ferretti, Alessandro, Claudio Prati, and Fabio Rocca. "Permanent scatterers in SAR interferometry." *Geoscience and Remote Sensing, IEEE Transactions on* 39.1 (2001): 8-20.

Fialko, Yuri, and Mark Simons. "Deformation and seismicity in the Coso geothermal area, Inyo County, California: Observations and modeling using satellite radar interferometry." *Journal of Geophysical Research B* 105.B9 (2000): 21781-21793.

Fialko, Yuri, Mark Simons, and Duncan Agnew. "The complete (3-D) surface displacement field in the epicentral area of the 1999 Mw7. 1 Hector Mine earthquake, California, from space geodetic observations." *Geophysical Research Letters* 28.16 (2001): 3063-3066.

Fournier, R. O., and J. M. Thompson. "The recharge area for the Coso." *California, geothermal system deduced from D and 18O in thermal and nonthermal waters in the region: US Geological Survey Open-File Report* (1980): 80-454.

Goldstein, Richard M., and Charles L. Werner. "Radar interferogram filtering for geophysical applications." *Geophysical Research Letters* 25.21 (1998): 4035-4038.

Goldstein, Richard M., Howard A. Zebker, and Charles L. Werner. "Satellite radar interferometry: Two-dimensional phase unwrapping." *Radio science* 23.4 (1988): 713-720.

Güler, Cüneyt, and Geoffrey D. Thyne. "Hydrologic and geologic factors controlling surface and

groundwater chemistry in Indian Wells-Owens Valley area, southeastern California, USA." *Journal of Hydrology* 285.1 (2004): 177-198.

Hole, J. K., et al. "Subsidence in the geothermal fields of the Taupo Volcanic Zone, New Zealand from 1996 to 2005 measured by InSAR." *Journal of volcanology and geothermal research* 166.3 (2007): 125-146.

Hooper, Andrew, P. Segall, and Howard Zebker. "Persistent scatterer interferometric synthetic aperture radar for crustal deformation analysis, with application to Volcán Alcedo, Galápagos." *Journal of Geophysical Research: Solid Earth* 112.B7 (2007).

"Indian Wells Valley groundwater basin." South Lahontan hydrologic region; California's Groundwater Bulletin 118.

Kaven, J. O., S. Hickman, and N. C. Davatzes. "MICRO-SEISMICITY, FAULT STRUCTURE AND HYDRAULIC COMPARTMENTALIZATION WITHIN THE COSO GETHERMAL FIELD, CALIFORNIA." *Proceedings, Thirty-Sixth Workshop on Geothermal Resrvoir Engineering*. 2011.

Lewis, J.C., "Fine-scale partitioning of contemporary strain in the southern Walker Lane: Implications for accommodating divergent strike-slip motion." Journal of Structural Geology 29 (2007) 1201-1215.

Liu, P., Li, Z., Hoey, T., Kincal, C., Zhang, J., Zeng, Q., and Muller, J., "Using advanced InSAR time series techniques to monitor landslide movements in Badong of the Three Gorges region, China." International Journal of Applied Earth Observation and Geoinformation 21 (2011): 253-264.

Massonnet, Didier, and Kurt L. Feigl. "Radar interferometry and its application to changes in the Earth's surface." *Reviews of geophysics* 36.4 (1998): 441-500.

Maxey, George B. "Hydrogeology of desert basins." *Ground Water* 6.5 (1968): 10-22.

Miller, M. Meghan, et al. "Refined kinematics of the Eastern California shear zone from GPS observations, 1993–1998." *Journal of Geophysical Research: Solid Earth* 106.B2 (2001): 2245-2263.

Mogi, Kiyoo. "Relations between the eruptions of various volcanoes and the deformations of the ground surfaces around them." (1958).

Monastero, F. C., et al. "The Coso geothermal field: A nascent metamorphic core complex." *Geological Society of America Bulletin* 117.11-12 (2005): 1534-1553.

Okada, Yoshimitsu. "Surface deformation due to shear and tensile faults in a half-space." *Bulletin of the seismological society of America* 75.4 (1985): 1135-1154.

Pluhar, Christopher J., et al. "Fault block kinematics at a releasing stepover of the Eastern California shear zone: Partitioning of rotation style in and around the Coso geothermal area and nascent metamorphic core complex." *Earth and Planetary Science Letters* 250.1 (2006): 134-163.

Reasenberg, Paul, William Ellsworth, and Allan Walter. "Teleseismic evidence for a low-velocity body under the Coso Geothermal Area." *Journal of Geophysical Research: Solid Earth* 85.B5 (1980): 2471-2483.

Romeiser, Roland, and Donald R. Thompson. "Numerical study on the along-track interferometric radar imaging mechanism of oceanic surface currents." *Geoscience and Remote Sensing, IEEE Transactions on* 38.1 (2000): 446-458.

“Rose Valley groundwater basin.” South Lahontan hydrologic region; California’s Groundwater Bulletin 118.

Ruch, J., et al. "Caldera-scale inflation of the Lazufre volcanic area, South America: Evidence from InSAR." *Journal of Volcanology and Geothermal Research* 174.4 (2008): 337-344.

Sarychikhina, Olga, Robert Mellors, and Ewa Glowacka. "Analysis of Spatial and Temporal Evolution of the Ground Deformation in the Cerro Prieto Geothermal Field (Mexicali Valley, BC, Mexico) Using DInSAR and Leveling Data." *Submitted to WGC* (2010).

SCEDC: Southern California Earthquake Center. Caltech Dataset. (2013). Doi:10.7909/C3WD3xH1.

“TSX (TerraSAR-X) Mission.” EOPortal Directory: European Space Agency. <https://directory.eoportal.org/web/eoportal/satellite-missions/t/terrasar-x>.

UofCal. California Weather Database: Haiwee Reservoir. Copyright 1998-2014. 05/10/2015. <ipm.ucdavis.edu>.

U.S. Geological Survey and California Geological Survey, Quaternary fault and fold database for the United States, 2006, accessed 10/29/2015, from USGS web site: <http://earthquakes.usgs.gov/regional/qfaults/>.

Walter, Allan W., and Craig S. Weaver. "Seismicity of the Coso Range, California." *Journal of Geophysical Research: Solid Earth* 85.B5 (1980): 2441-2458.

Wangensteen, Bjørn, Dan Johan Weydahl, and Jon Ove Hagen. "Mapping glacier velocities on Svalbard using ERS tandem DInSAR data." *Norsk Geografisk Tidsskrift* 59.4 (2005): 276-285.

Wicks, C.W., Thatcher, W., Monastero, F.C., and Hasting, M.A., “Steady state deformation of the Coso Range, east central California, inferred from satellite radar interferometry.” Journal of Geophysical Research, Vol. 106.B7 (2001):13769-13780.

Williams, A. E., and M. A. McKibben. "Isotopic and chemical constraints on reservoir fluids

from the Coso Geothermal Field, California." *Geothermal Resources Council. Transactions* 14 (1990): 1545-1552.

Yang, Xue-Min, Paul M. Davis, and James H. Dieterich. "Deformation from inflation of a dipping finite prolate spheroid in an elastic half-space as a model for volcanic stressing." *Journal of Geophysical Research: Solid Earth* 93.B5 (1988): 4249-4257.

Zebker, Howard A., and Richard M. Goldstein. "Topographic mapping from interferometric synthetic aperture radar observations." *Journal of Geophysical Research: Solid Earth* 91.B5 (1986): 4993-4999.

Zhang, G., Shan, X., Delouis, B., Qu, C., Balestra, J., Li, Z., Liu, Y., and Zhang, G., “Rupture history of the 2010 M_s 7.1 Yushu earthquake by joint inversion of teleseismic data and InSAR measurements.” *Tectonophysics* 584 (2013): 129-137.